이학박사학위논문

Evolution of microstructures and fluid inclusions of naturally deformed peridotites: Implications for physico-chemical heterogeneity in the upper mantle

자연 상에서 변형된 감람암의 미세구조와
유체포유물의 진화사: 상부맨틀의 물리화학적
불균질성에 관한 의의

2017 년 2 월

서울대학교 대학원

지구환경과학부

박 문 재

Evolution of microstructures and fluid inclusions of naturally deformed peridotites: Implications for physico-chemical heterogeneity in the upper mantle

지도교수 정 해 명

이 논문을 이학박사 학위논문으로 제출함

2016 년 12 월

서울대학교 대학원

지구환경과학부

박 문 재

박문재의 이학박사 학위논문을 인준함

2016 년 12 월

위 원 장 이 인 성 (인)

부위원장 정 해 명 (인)

위 원 길 영 우 (인)

위 원 이 준 기 (인)

위 원 김 덕 진 (인)

Doctoral Thesis

Evolution of microstructures and fluid inclusions of naturally deformed peridotites: Implications for physico-chemical heterogeneity in the upper mantle

Munjae Park

A dissertation submitted in partial fulfillment of the requirements for the degree of Doctor of Philosophy

School of Earth and Environmental Sciences
Seoul National University

February 2017

ABSTRACT

Evolution of microstructures and fluid inclusions of naturally deformed peridotites: Implications for physico-chemical heterogeneity in the upper mantle

Munjae Park
School of Earth and Environmental Sciences
The Graduate School
Seoul National University

The Earth's uppermost layer, the lithosphere, consists of the crust and upper mantle, in particular, the lithospheric mantle is the space that physically and chemically forms the roots of crust. Mantle-derived peridotites can provide important information about the physico-chemical properties of the upper mantle (i.e., mantle metasomatisms and deformation processes), thus, it plays an important role in understanding Earth's geochemical and rheological evolutionary processes.

In this dissertation, naturally deformed peridotites (xenolith and massif type) were studied using various analytical instruments (SEM-EBSD, EPMA, FTIR-Raman spectroscopy, FIB, Heating-Cooling stage, etc.) in order to understand how deformation microstructures and fluid inclusions were evolved from Rio Grande Rift (New Mexico, USA) and Yugu area (Gyeonggi Massif, Korea).

Five spinel peridotite xenoliths, hosted in alkali basalts, were collected from Adam's Diggings in the western margin of the Rio Grande Rift (RGR), New Mexico, USA. Based on fluid inclusion petrography, two distinct generations of fluid inclusion assemblages, both hosted by orthopyroxenes, namely Type-1 (earlier) and Type-2 (later) FIs, were identified. Results from fluid inclusion petrography together with various analytical results indicated that the timing of the entrapment and the composition of the trapped fluid were different between the Type-1 and Type-2 FIs.

All of these results indicate that there were at least two fluid invasions with different fluid compositions at different pressures (depth) beneath the RGR mantle. The earlier fluid invasion (C–O–N–S) happened before or during formation of exsolution lamellae and was trapped as Type-1 FI in the cores of orthopyroxenes whereas the later fluid invasion (C–O–H–S) was trapped as Type-2 FI after the formation of the orthopyroxene porphyroclasts with exsolution lamellae. The two fluid invasions in the Adam's Diggings peridotites indicate the complexity of mantle fluids around the RGR.

Transitional characteristics of microstructures and olivine fabrics developed in a mantle shear zone from the Yugu peridotite body (Gyeonggi Massif, Korea) were studied. The Yugu peridotite body predominantly comprises spinel harzburgite together with minor lherzolite, dunite, and clinopyroxenite. Based on microstructural characteristics of highly deformed peridotites, we classified into proto-mylonite, proto-mylonite to mylonite transition, mylonite, and ultra-mylonite. Olivine fabrics changed from A-type (proto-mylonite) via D-type (mylonite) to E-type (ultra-mylonite). Olivine fabric transition is interpreted as occurring under hydrous conditions at low temperature and high strain, because of characteristics such as Ti-clinohumite defects (and serpentine) and fluid inclusion trails in olivine, and a hydrous mineral (pargasite) in the matrix, especially in the ultra-mylonitic peridotites.

Keywords: peridotite, fluid inclusion, microstructures, mantle metasomatism, mantle evolution, mantle heterogeneity

Student Number: 2011-30116

TABLE OF CONTENTS

CHAPTER 3. Microstructural evolution of the Yugu peridotites in the Gyeonggi Massif, Korea: Implications for olivine fabric transition in mantle shear zones

CHAPTER 1

Introduction

In general, the upper mantle consists of peridotite with 50–60% olivine, 20–30% pyroxenes, and 15–25% garnet (Ringwood, 1979). Mantle heterogeneity is closely related to the distribution of volatile components and volatile cycles in the Earth's interior, and understanding the role of volatiles in deep mantle processes is one of the key issues in mantle petrology (Litasov *et al.*, 2013). The lithospheric mantle in subduction zone can be considered as an important reservoir for various volatiles (Fig. 1.1) (i.e., C–O–H–N–S system) (Taylor & Green, 1988; Holloway & Blank, 1994), and these volatiles in subduction zone play also critical roles in interaction with the lithospheric mantle causing fluid/melt-induced mantle metasomatism (Belkin & De Vivo, 1989; Schiano *et al.*, 1992; O'Reilly & Griffin, 2000) and metamorphism (Peacock, 1990; Bebout, 2007).

Another important issue related to the behavior of volatiles in the mantle is the influence of hydrogen and carbon on the rheological and transport properties of silicates (Litasov *et al.*, 2013 and references therein). Based on experimental studies, rheological properties of minerals and rocks change dramatically with a number of parameters (Karato *et al.*, 2008)

including stress (strain-rate), temperature, pressure, water content and grain size, thus these are the key to the understanding of dynamics and evolution of mantle. Comparing between natural and experimental works is necessary to understand physico-chemical evolution of mantle because rheological properties and behavior of volatiles in nature are more complicated than those from laboratory or theoretical studies. Some of major tools for solving these issues are studies of deformation microstructures (Jung *et al.*, 2009; Skemer *et al.*, 2010; Soustelle *et al.*, 2010; Skemer *et al.*, 2013) and fluid inclusions (Hidas *et al.*, 2010; Katayama *et al.*, 2010; Berkesi *et al.*, 2012; Frezzotti *et al.*, 2012a; Kawamoto *et al.*, 2012; Kawamoto *et al.*, 2013) from naturally deformed peridotites. Therefore, study on microstructures and fluid inclusions can give rheological and geochemical information for understanding the origin and evolution history of upper mantle rocks related to geodynamics. However, the combined study between microstructures and fluid inclusions is rare in both naturally and experimentally deformed peridotites.

In this doctoral thesis, therefore, I concentrate on evolution of the fluid inclusions and deformation microstructures from both upper mantle rocks (peridotite xenoliths and massive peridotite body) related to specific geodynamics (rift, subduction, and collision zones). These rock samples were collected from Rio Grande rift in New Mexico (U.S.A.) and Yugu area in the Gyeonggi Massif (Korea). Two main subjects for doctoral thesis are followed:

(1) Fluid invasions in the lithospheric upper mantle based on fluid inclusion study in spinel peridotites from Adam's Diggings, Rio Grande Rift, U.S.A. (Chapter 2); (2) Microstructural evolution of the Yugu peridotites in the Gyeonggi Massif, Korea: Implications for olivine fabric transition in mantle shear zones (Chapter 3). These studies can provide physico-chemical heterogeneity of upper mantle related to rifting, subduction, and collision processes, and how these different fluids and deformation microstructures were evolved during these processes.

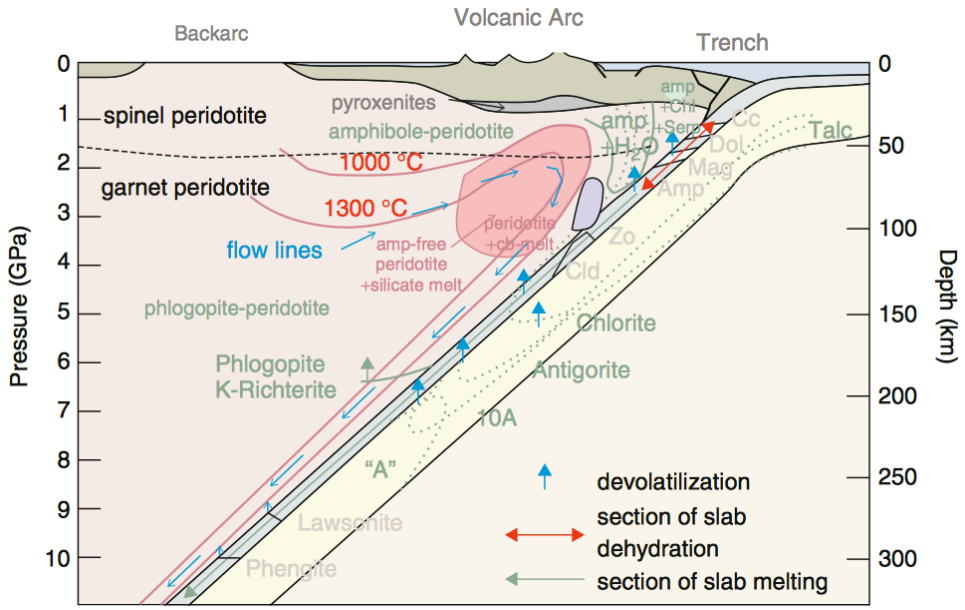

Fig. 1.1. Schematic illustration of devolatilization, dehydration reactions, and melting in subduction zones (Keppler, 2013). A series of dehydration reactions in the sediments, altered basalts and in the serpentinized peridotites of the subducting slab releases hydrous fluids that infiltrate into the mantle wedge.

CHAPTER 2

Fluid invasions in the lithospheric upper mantle based on fluid inclusion study in spinel peridotites from Adam's Diggings, Rio Grande Rift, U.S.A.

Abstract

Spinel peridotite xenoliths, hosted in alkali basalts (~15 Ma), were collected from Adam's Diggings in the western margin of the Rio Grande Rift (RGR), New Mexico, USA. We selected five representative spinel peridotite xenoliths that had abundant in fluid inclusions (FIs). Based on fluid inclusion petrography, two distinct generations of fluid inclusion assemblages, both hosted by orthopyroxenes, namely Type-1 (earlier) and Type-2 (later) FIs, were identified. Results from fluid inclusion petrography together with various analytical results (microthermometry, high-resolution Raman micro-spectroscopy, and focused ion beam-scanning electron microscopy) indicated that the timing of the entrapment and the composition of the trapped fluid were different between the Type-1 and Type-2 FIs. All of these results indicate that there were at least two fluid invasions with different fluid compositions at different pressures (depth) beneath the RGR mantle. The earlier fluid invasion (C–O–N–S) happened before or during formation of exsolution lamellae and was trapped as Type-1 FI in the cores of orthopyroxenes whereas the later fluid invasion (C–O–H–S) was trapped as

Type-2 FI after the formation of the orthopyroxene porphyroclasts with exsolution lamellae. The two fluid invasions in the Adam's Diggings peridotites indicate the complexity of mantle fluids around the RGR. During the ascent of the xenoliths, post-entrapment reactions produced magnesite and quartz in Type-1 FIs and magnesite and talc in Type-2 FIs as reaction products of the fluid and its host mineral (orthopyroxene).

Keywords: fluid inclusions; mantle xenoliths; mantle metasomatisms; Adam's Diggings; Rio Grande Rift

2.1. Introduction

The lithospheric mantle can be considered to be an important reservoir for various volatiles because of the presence of volatile species of the C–O–H–N–S system that has been recognized in the last few decades (Taylor & Green, 1988; Holloway & Blank, 1994; Wyllie & Ryabchikov, 2000; Frezzotti & Touret, 2014) through the discovery of (1) volatile-bearing minerals such as amphibole and mica (Dawson & Powell, 1969; Dawson & Smith, 1982) and/or (2) fluid inclusions in upper mantle xenoliths and peridotite bodies (Török & De Vivo, 1995; Szabó & Bodnar, 1996; Andersen & Neumann, 2001; Frezzotti, 2001; Sachan *et al.*, 2007; Hidas *et al.*, 2010; Berkesi *et al.*, 2012; Frezzotti *et al.*, 2012a). The presence of C–O–H–N–S in fluid inclusions hosted by mantle xenoliths is represented mainly by CO_2-rich fluid with minor components such as H_2O, N_2, CH_4, CO, and H_2S at either room temperature (Roedder, 1965; Murck *et al.*, 1978; Bergman & Dubessy, 1984; Pasteris, 1987; Huraiova *et al.*, 1991; Andersen *et al.*, 1995; Yamamoto *et al.*, 2002; Sachan *et al.*, 2007; Frezzotti *et al.*, 2010; Kawamoto *et al.*, 2013; Berkesi *et al.*, 2016) or moderately elevated temperatures (Berkesi *et al.*, 2009; Hidas *et al.*, 2010). Moreover, the presence of Cl-rich fluid inclusions in lithospheric mantle has also been reported (Izraeli *et al.*, 2001; Konzett *et al.*, 2014), revealing the complexity of mantle fluids.

The Rio Grande Rift (RGR) is one of the world's best exposed and most thoroughly studied examples of a continental rift system (Ricketts *et al.*,

2016). Numerous studies have focused on understanding melting and/or metasomatic processes in the mantle by investigating alkali and tholeiitic basalts (Perry *et al.*, 1987), ultrapotassic magmas (Gibson *et al.*, 1993), basaltic melt inclusions (Rowe & Lassiter, 2009; Rowe *et al.*, 2015), pyroxenite xenoliths (Porreca *et al.*, 2006), and peridotite xenoliths (Smith, 2000; Kil & Wendlandt, 2004; 2007; Byerly & Lassiter, 2012; 2015). The latter studies (i.e., peridotite xenoliths) generally used major, trace, and isotopic compositions as major tools for tracing and modeling mantle metasomatism. However, fluid inclusion studies on RGR mantle xenoliths have been lacking so far, despite the fact that fluid/melt inclusions are powerful tools for gaining insight into the nature of cryptic metasomatism (Andersen *et al.*, 1984; Menzies *et al.*, 1987; Belkin & De Vivo, 1989; Schiano *et al.*, 1992; Schiano & Clocchiatti, 1994; O'Reilly & Griffin, 2000; Szabó *et al.*, 2009; Hidas *et al.*, 2010; Berkesi *et al.*, 2012; Frezzotti & Touret, 2014).

Despite the importance of fluid inclusions study, to our best knowledge, high-density CO_2 inclusions only in xenoliths from Kilbourne Hole (located at the rift axis of the RGR) have been reported (Roedder, 1965) so far. Therefore, in this paper, we report a detailed study on fluid inclusions hosted by mantle xenoliths from Adam's Diggings located at the western margin of RGR using microthermometry, high-resolution Raman micro-spectroscopy, and focused ion beam-scanning electron microscopy. Finally, we provide a relationship between Type-1 (earlier) and Type-2 (later) fluid

inclusion generations with possible mantle metasomatic event(s). Our results shed light on a complexity of mantle fluids beneath the western margin of RGR (Adam's Diggings).

2.2. Geology and sampling

As one of the world's principal Cenozoic continental rift systems, the RGR extends for more than 1000 km from Colorado through New Mexico to Mexico (located mostly between the Colorado Plateau and the Great Plains) (Fig. 2.1). The timing and locations of crustal shortening, magmatism, compression, and extension processes in the western USA has been explained by interactions between the North American and Farallon plates (Severinghaus & Atwater, 1990). During the Laramide orogeny (ca. 80–40 Ma), shallow subduction resulted in compression, crustal shortening, and uplift of large regions (e.g., the Colorado Plateau) (Dickinson & Snyder, 1978). Then, Farallon slab delamination (~37 Ma) and rollback (~28 Ma) processes caused an influx of hot asthenospheric mantle beneath the previously cooled continental lithospheric mantle and a transition from compressional to extensional tectonics with mafic volcanisms (Humphreys, 2009; Copeland *et al.*, 2011). Additionally, the subducting Farallon plate hydrated the base of the overlying North American Plate (Humphreys *et al.*, 2003). The development of the RGR is considered to consist of an early rifting (Oligocene to middle Miocene; 37–15 Ma) and a late rifting stage (middle

Miocene to Holocene; 15–0 Ma). According to Kil and Wendlandt (2007), spinel peridotite xenoliths from the rift shoulder (Adam's Diggings) show strong metasomatic characteristics and also evidence of partial melting related to the subducted Farallon oceanic plate. The Farallon slab delamination and rollback processes are considered to have occurred during the early rifting process. During the late rifting, localized alkali basalt magmas erupted in the Adam's Diggings (Fig. 2.1) brought mantle xenoliths to the surface during the time period between 13 and 6 Ma.

From previously collected spinel peridotite xenoliths (lherzolite and harzburgite) from the Adam's Diggings regions beneath the western margin of RGR (Fig. 2.1), we selected five spinel peridotite xenoliths that were abundant in fluid inclusions (Table 2.1). These xenoliths were the subject of detailed petrological and geochemical studies examining their pressure and temperature conditions (Kil & Wendlandt, 2004) and metasomatic processes (Kil & Wendlandt, 2007); however, the fluid inclusions in these mantle xenoliths had not been described. These xenoliths have porphyroclastic textures and have undergone deformation related to the rifting process (Park *et al.*, 2014). They consist of olivine, orthopyroxene, clinopyroxene, and spinel. In addition, xenoliths ADTM18, ADTM27, and ADTM37 contained 0.1 vol. %, 4 vol. %, and 0.1 vol. % of phlogopite (Table 2.1), respectively, as an indicator of modal metasomatism. Exsolution lamellae of clinopyroxene in the orthopyroxene porphyroclasts (Fig. 2.2a–c) is commonly observed and was interpreted as having formed prior to xenolith ascent to the surface,

indicating a cooling event in the subcontinental lithospheric mantle beneath the Adam's Diggings (Kil & Wendlandt, 2004). A summary of the petrographic results, such as modal composition, lithology, textures, and equilibrium temperatures is provided in Table 2.1.

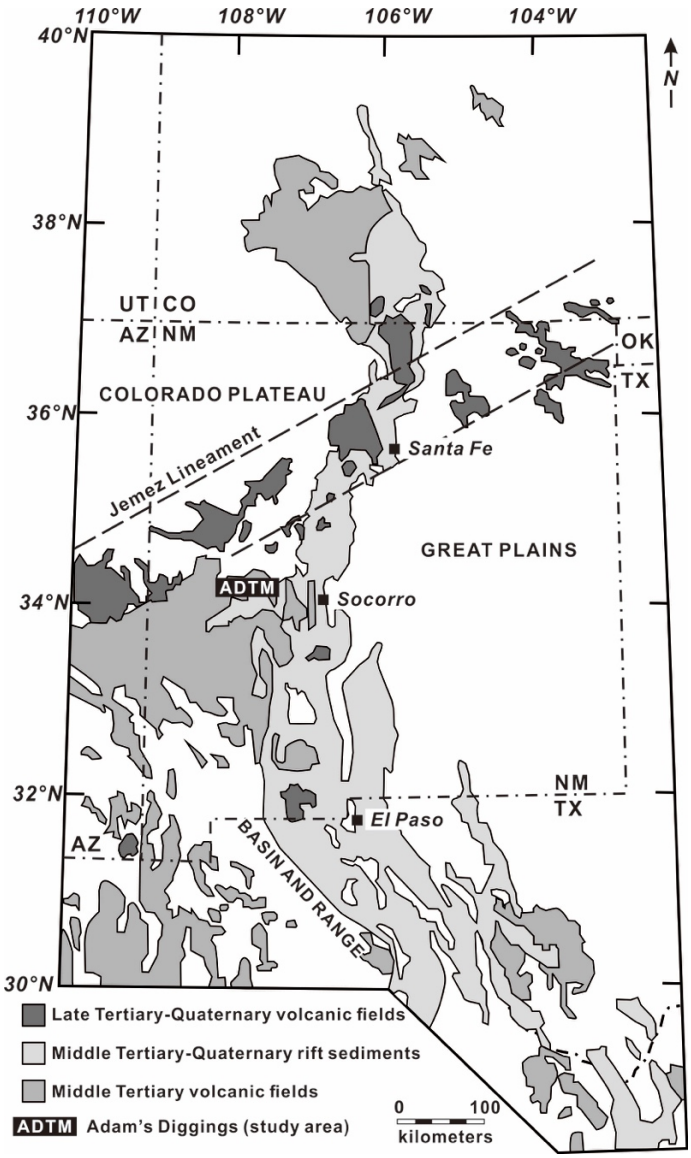

Fig. 2.1. Simplified geological map in the Rio Grande Rift, New Mexi co, USA (modified after Hudson & Grauch, 2013). The black rectang ular box represents the study area (ADTM: Adam's Diggings) on the rift shoulder. The dashed-dotted lines indicate US state boundaries. Da shed lines show the position of the Jemez lineament. Abbreviations: A Z, Arizona; CO, Colorado; NM, New Mexico; OK, Oklahoma; TX, T exas; and UT, Utah.

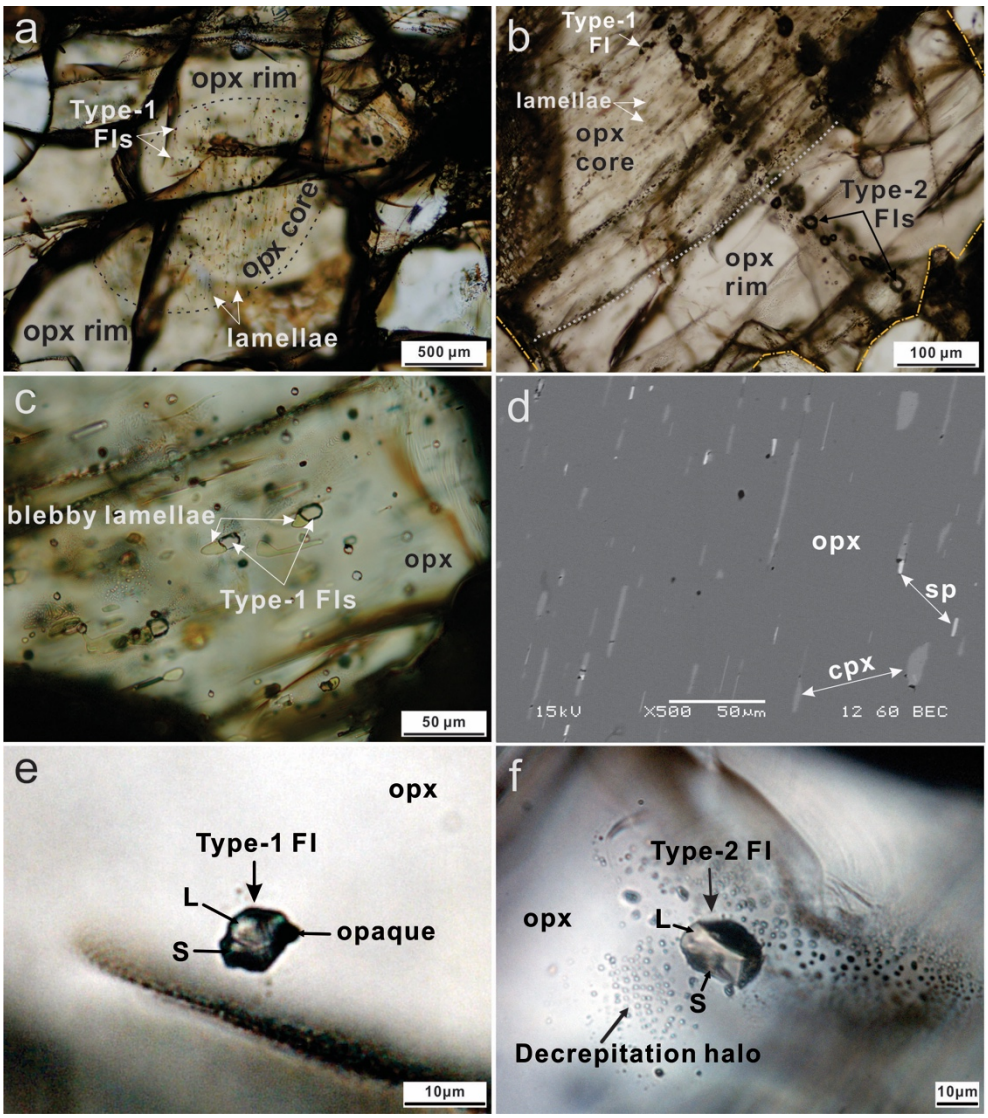

Fig. 2.2. Optical photomicrographs (a-c, e, and f) and a backscattered electron (BSE) image (d), showing the main petrographic features of fluid inclusions from the studied ADTM xenoliths. (a) Photomicrograph showing an orthopyroxene porphyroclast with a lamellae and inclusion-rich core and a lamellae and inclusion-free rim (xenolith ADTM13). (b) Photomicrograph showing an orthopyroxene porphyroclast with a lamellae-rich and inclusion-rich core and with a lamellae-free and inclusion-free rim, where the entire

orthopyroxene grain is crosscut by negative crystal-shaped Type-2 FIs generation (xenolith ADTM27). Dashed-dotted lines denote the edge of the host crystal. (c) Photomicrograph showing the petrographic relationships of the Type-1 FIs (fluid inclusions) and also blebby lamellae (likely clinopyroxene). The Type-1 FIs generally occur as individual fluid inclusions; however, in some cases, they appear adhered to a blebby lamella, indicating the presence of fluid during lamellae formation (xenolith ADTM18). (d) BSE image of the lamellae-rich area in the porphyroclastic orthopyroxene core (xenolith ADTM27). (e) Representative image of a negative crystal shape Type-I FI showing three visible phases at room temperature: an opaque, a translucent solid (S) and a liquid phase (L) (xenolith ADTM07). (f) Type-2 FI showing negative crystal shape and occurring along healed fractures. This inclusion is decrepitated and contain two phases: solid (S) and liquid (L) at room temperature (xenolith ADTM37).

Table 2.1. Modal composition, lithology, texture, equilibrium temperature, pre-eruption depth range, and oxygen fugacity in the studied spinel peridotite xenoliths (Adam's Diggings) from the Rio Grande Rift.

Xenoliths	Modal composition (%)					Lithology	Texture	T (°C) (cpx-opx[a])	T (°C) (Ca-in-opx[a])	Pre-eruption depth range[b]	fO_2[c]
	Ol	Opx	Cpx	Sp	Phl						
ADTM07	66	20	12	2		Sp-Hzb	Po	960	980		-0.1812
ADTM13	80	12	7	2		Sp-Lhz	Po	970	960		0.4457
ADTM18	67	24	8	1	trace	Sp-Hzb	Po	1000	970	39–60 km	0.6539
ADTM27	78	6	14	3	4	Sp-Lhz	Po	1030	970		0.2212
ADTM37	78	12	8	1	trace	Sp-Hzb	Po	1010	870		0.4296

ADTM: Adam's Diggings; Ol: olivine; Opx: orthopyroxene; Cpx: clinopyroxene; Sp: spinel; Phl: phlogopite; Hzb: harzburgite; Lhz: lherzolite; Po: porphyroclastic texture.

[a]Equilibrium temperature calculated by two-pyroxene and Ca-in-opx of Brey & Köhler (1990) at 15 kb, st.dev ± 16°C.

[b]Pre-eruption depth range based on upper mantle structure and textures (Kil & Wendlandt, 2004).

[c]Oxygen fugacity values calculated by Ballhaus *et al.* (1991) at 15 kb.

2.3. Analytical techniques

Double-polished thick sections (thickness of about 100 microns) were prepared from the xenoliths, and we selected various fluid inclusions close to the surface (<10 μm) for further study.

Microthermometric data were collected using a Linkam THMS600 heating-cooling stage mounted on a Nikon Eclipse LV100PL polarizing microscope at the Lithosphere Fluid Research Lab, Eötvös University, Budapest. For calibration, we used the melting point of CO_2 of –56.6 ºC, with an accuracy of measurement of ±0.1 ºC. The fluid inclusions were cooled to –150 ºC, beyond having reached complete freezing, and then were slowly heated until visible total homogenization occurred. The density and minimum pressure values of the fluids were estimated using the FLUIDS software package (BULK & ISOC) (Bakker, 2003).

Micro-Raman analysis was conducted to determine fluid components at the Faculty of Science Research and Instrument Core Facility of Eötvös University, Budapest (ELTE FS-RICF). We used a confocal HORIBA Labram HR (high resolution) 800 spectrometer with Nd-YAG laser (λ=532 nm) excitation, an 1800 gr/mm optical grating, a 50–200 μm confocal hole, a 2–150 sec acquisition time, and a 100× objective. The laser spot size (lateral) was measured to be 1.17 μm, and the depth resolution was 1.73 μm (using a 50 μm confocal hole and 100× objective). The laser power was 100 mW at the source and ~50 mW at the sample surface. The spectral resolution was 0.7

cm^{-1} at 1398.5 cm^{-1} (full width at half maximum of one neon line). We followed the method of Berkesi *et al*. (2009) for detecting small amounts of water in fluid inclusions. Data evaluation (background fitting and peak fitting using the Gaussian–Lorentzian function) was carried out using LabSpec software. For mineral and fluid identification, the databases by Frezzotti *et al.* (2012b) as well as RRUFF (rruff.info) were used.

At ELTE FS-RICF, focused ion beam–scanning electron microscopy (FIB–SEM) analysis was also conducted using a FEI QUANTA 3D FIB–SEM apparatus equipped with both secondary and backscattered electron (BSE) detectors, together with a silicon drift energy dispersive spectrometer (EDS). Fluid inclusions with size in the range 5–25 μm and within a few micrometers (not more than 5 μm) of the host mineral surface were selected for FIB–SEM analysis. The accelerating voltage and current of the electron beam were 20 kV and 10 nA, respectively, which allowed major elements having masses ranging from those of beryllium through oxygen to barium to be analyzed. Identification of daughter phases was based mostly on their morphology on the secondary and on their brightness on the backscattered electron images together with examination of EDS spectra. Because of the small size of the daughter phases in the inclusions (1–5 μm), the signals detected by EDS were mixed signals, as X-rays from adjacent areas (host phase and/or other daughter minerals) were also recorded. To distinguish the daughter phase signal from that of the host mineral better, EDS control spectra for the host mineral were also acquired in the proximity of and from the same depth as

the solid phases after each acquisition of daughter mineral spectrum. The detailed methodology for this technique was described in Berkesi *et al.* (2012). The size of slices for fluid inclusions was set to 200 nm.

In order to obtain the major-element composition of core orthopyroxenes and enclosed lamellae, electron microprobe analysis (EPMA) was conducted using a wavelength- dispersive JEOL JXA-8100 electron-microprobe at Gyeongsang National University with instrument settings of 15 kV accelerating voltage, 10 nA beam current, 1 μm beam size, and 20 s counting times. Natural standards were used for the analyses and ZAF correction was applied.

Volume percentages of the clinopyroxene and spinel lamellae in the orthopyroxene were calculated on each studied sample using 1-3 representative BSE images on the lamellae- bearing core of orthopyroxene (e.g., Fig. 2.2d). Image resolutions were 254 dpi with a pixel number of 1280x960. Corel PHOTO-PAINT v.X8 was used to calculate the pixel numbers of the phases. The pixel numbers of all clinopyroxene, relative to the total pixel numbers of the whole image, gave the vol.% of clinopyroxene; the same approach was used for spinel and the core of orthopyroxene.

2.4. Fluid inclusion petrography

Two generations of fluid inclusions (FIs), all enclosed in orthopyroxenes and mostly in deformed porphyroclasts (Fig. 2.2), were

distinguished. Based on our observations, exsolution lamellae always present in the core of the porphyroclastic orthopyroxenes (Fig. 2.2a and b) including lamellar spinel (Fig. 2.2a–d) as well as blebby clinopyroxenes (Fig. 2.2c and d). One fluid inclusion generation (assemblage) has been identified as either following the orientation of lamellae or adhering to one lamella (Fig. 2.2c). This fluid inclusion assemblage (hereafter referred to as Type-1; Fig. 2.2c and e) is generally present only together with lamellae, thus the lamellae-free rim of orthopyroxene host does not contain Type-1 FIs. However, there is no mutual occurrence of the lamellae and the Type-1 FIs as there are numerous lamellae-bearing orthopyroxenes without any associated fluid inclusions. The size of Type-1 FIs varies between 2 and 10 μm, and these inclusions dominantly show one (liquid) or two visible phases (liquid and solid) at room temperature (Fig. 2.2c and e). These inclusions are characterized by rather undisturbed features as no visible signs of stretching and/or decrepitation were observed (Fig. 2.2c and e). Type-1 FIs sometimes appear together with an opaque solid phase adhered to the edge of the individual fluid inclusion (Fig. 2.2e).

Another type of FI assemblage (hereafter referred to as Type-2, Fig. 2.2b and f) appears along healed fractures of orthopyroxene porphyroclasts reaching the edge of the host mineral (Fig. 2.2b) and crosscutting Type-1 FIs (Fig. 2.2b). The size of these inclusions varies within a wide range from 10 to 100 μm (Fig. 2.2f), and the inclusions contain two (liquid, solid) or three (vapor, liquid, solid) phases at room temperature (Fig. 2.2f). This type of

inclusion is typically decrepitated and thus is connected to numerous small fluid inclusions forming halos (Fig. 2.2f) showing petrographic evidence for re-equilibration of the fluid inclusions.

2.5. Microthermometry

Microthermometry was conducted on both the Type-1 (n = 94) and the Type-2 (n = 58) FIs from the five selected spinel peridotite xenoliths (Table 2.2). Detailed microthermometric data is shown in Table 2.3. Upon progressive heating, the first phase transition detected was the melting of a solid phase in the presence of a vapor bubble to liquid. The melting temperatures (T_m) of this solid phase showed slightly lower ranges in the Type-1 FIs (–58.0 to –57.0 ºC) than in the Type-2 FIs (–57.1 to –56.8 ºC) (Table 2.3). These data indicate the predominance of CO_2 in the fluid phases within both types of fluid inclusions. Moreover, the melting point depression from that of pure CO_2 (determined to be –56.6 ºC) suggests the presence of minor amounts of other components (e.g., Roedder, 1984; van den Kerkhof, 1988; Frezzotti *et al*., 2002). After the solid phase was made molten, only the liquid and the vapor phases were observed together until further heating resulted in homogenization. Attainment of the homogenization temperature (T_h) of the liquid and vapor phases always resulted in a liquid phase. Both of the cases of Type-1 and Type-2 FIs showed a wide range of T_h: –42.0 to –9.5 ºC and 9.6 to 25.5 ºC (Table 2.3 and Fig. 2.3), respectively. Density for both types was calculated on the basis of homogenization temperatures (T_h, Table

2.3), using the equation of state developed by Span & Wagner (1996), approximated by pure CO_2 system. The calculated CO_2 density (for pure CO_2) for the Type-1 and Type-2 FIs was 0.98–1.12 g/cm^3 and 0.70–0.86 g/cm^3 (Table 2.3), respectively. Thus, the T_h range and the calculated CO_2 density of the two types of FIs clearly differ from each other without any overlap.

2.6. Raman microspectrometry

For the five selected spinel peridotite xenoliths, micro-Raman analysis was conducted to identify the compositions of the fluid and solid phases more precisely in each type of fluid inclusions (Type-1: n = 50; Type-2: n = 50) (Table 2.2). The results confirmed the data provided by microthermometry, namely, that the Type-1 and Type-2 FIs contain dominantly CO_2. These two types of fluid inclusions were always detected with a CO_2-rich liquid phase (the Fermi diad bands; Raman shift values at ~1281 cm^{-1} and ~1386 cm^{-1} for Type-1 FIs and ~1282 cm^{-1} and ~1386 cm^{-1} for Type-2 FIs) (Fig. 2.4a and c).

2.6.1. Type-1 FIs

Due to the attainable spectral resolution of the Raman instrument, we could detect both the nitrogen linked to the fluid phase as well as that in the air (e.g., Berkesi *et al*., 2016) . This was represented by a kind of doublet peak on the spectrum in the spectral region around 2330 cm^{-1} (Fig. 2.4b). Nitrogen

in the air was also detected when measuring the sample off, but close to the inclusion at the same depth in the sample and with the same parameters used for the inclusion beforehand. The nitrogen peak that was found when measuring only fluid inclusion always appeared at lower wavenumber than that of nitrogen in the air (Fig. 2.4b): ~2327.3 cm^{-1} in the fluid; ~2330.7 cm^{-1} in the air (Fig. 2.4b).

An opaque solid phase in Type-1 FIs (Fig. 2.2e) was most likely a sulfide phase having a Raman peak at 472.5 cm^{-1} (Fig. 2.4a). The characteristic peaks of a Mg-carbonate (magnesite) (738.2 cm^{-1} and 1095.5 cm^{-1}) were also found (Fig. 2.4a).

2.6.2. Type-2 FIs

For the Type-2 FIs, peaks of dissolved H_2O in CO_2 (at ~3636.1 cm^{-1}) were clearly shown (Fig. 2.4d). This figure also demonstrates that the peak intensity for the H_2O increased with increasing temperature, a result similar to that described in a study by Berkesi *et al*. (2009) for detection of small amounts of H_2O in CO_2-rich fluid inclusions. Aside from the dissolved H_2O peak, the Type-2 FIs also showed the presence of a OH-bearing solid phase, namely talc (~3676.2 cm^{-1} in Fig. 2.4d). Similar to the case of the Type-1 FIs, the presence of magnesite was also observed (peaks at 212.2 cm^{-1}, 329.2 cm^{-1}, and 1094.4 cm^{-1} in Fig. 2.4c).

Table 2.2. Number of measurements of the applied analytical techniques in the studied spinel peridotites (Adam's Diggings) from the Rio Grande Rift.

Xenoliths	Types (FIA)	Number of measurements (n)		
		Microthermometry	Raman microspectrometry	FIB-SEM
ADTM07	Type-1	16	9	
	Type-2	11	9	
ADTM13	Type-1	18	10	
	Type-2	10	10	
ADTM18	Type-1	17	9	2
	Type-2	12	10	2
ADTM27	Type-1	21	11	2
	Type-2	13	11	2
ADTM37	Type-1	22	11	2
	Type-2	12	10	2
Total	Type-1	94	50	6
	Type-2	58	50	6

Table 2.3 Details of petrography, microthermometry, and Raman spectroscopy of the studied fluid inclusions.

Types (FIA)	Xenoliths	Host minerals	Size (μm)	Shape	Phases (room T)	Fluid phases	T_m (°C)	T_h (°C)	ρ (g/cm^3)[a]	Solid phases
Type-1 (n=94)	ADTM07	Opx	2–10	Negative crystal shape	(L+S)	CO_2–N_2	-57.8 – -57.3	-30.5 – -16.0	1.02 – 1.08	Magnesite, quartz, sulfide
	ADTM13						-58.0 – -57.4	-32.5 – -11.0	0.99 – 1.09	
	ADTM18						-57.6 – -57.0	-40.5 – -19.5	1.03 – 1.12	
	ADTM27						-58.0 – -57.2	-42.0 – -15.5	1.01 – 1.12	
	ADTM37						-57.9 – -57.0	-33.3 – -9.5	0.98 – 1.09	
Type-2 (n=58)	ADTM07	Opx	10–100	Negative crystal shape	(L+S) or (V+L+S)	CO_2–H_2O	-57.0 – -56.8	9.8 – 22.6	0.74 – 0.86	Magnesite, talc, sulfate, Fe-Ni oxide
	ADTM13						-57.1 – -56.9	13.6 – 25.5	0.70 – 0.83	
	ADTM18						-57.1 – -56.8	11.5 – 21.5	0.76 – 0.85	
	ADTM27						-57.0 – -56.8	9.6 – 22.8	0.74 – 0.86	
	ADTM37						-57.1 – -56.9	12.5 – 23.6	0.73 – 0.84	

n: number of measurements; Opx: orthopyroxene; L: liquid; S: solid; V: vapor; Tm: melting temperature; Th: homogenization temperature.

[a] The CO_2 density in fluid inclusions calculated by the FLUIDS software package (BULK) (Bakker, 2003).

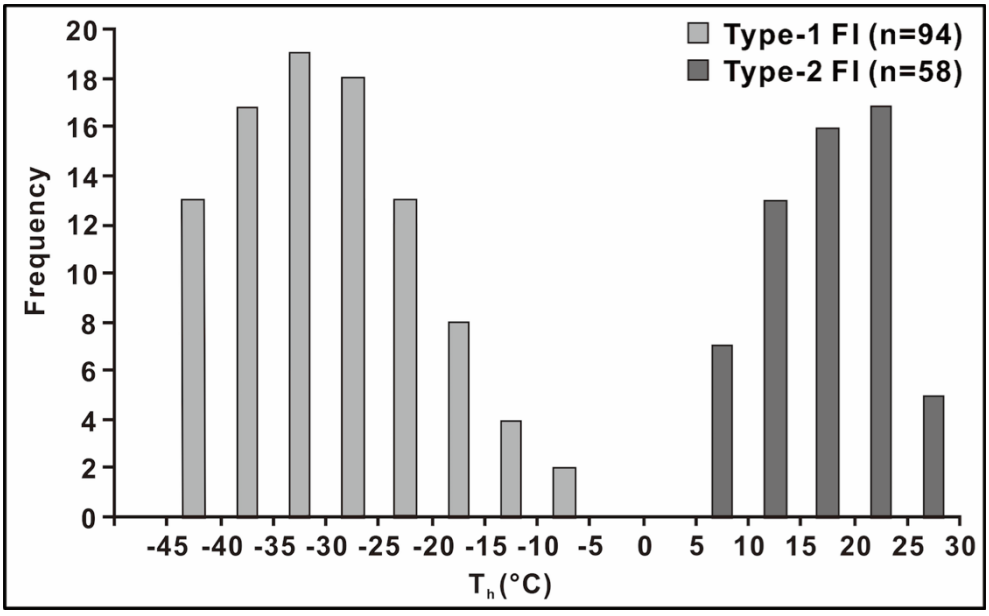

Fig. 2.3. The histogram showing homogenization temperatures (T_h) for two distinct CO_2-rich fluid inclusion generations (Type-1 and Type-2 FIs) occurring orthopyroxenes. n: the number of measurement for each fluid inclusion.

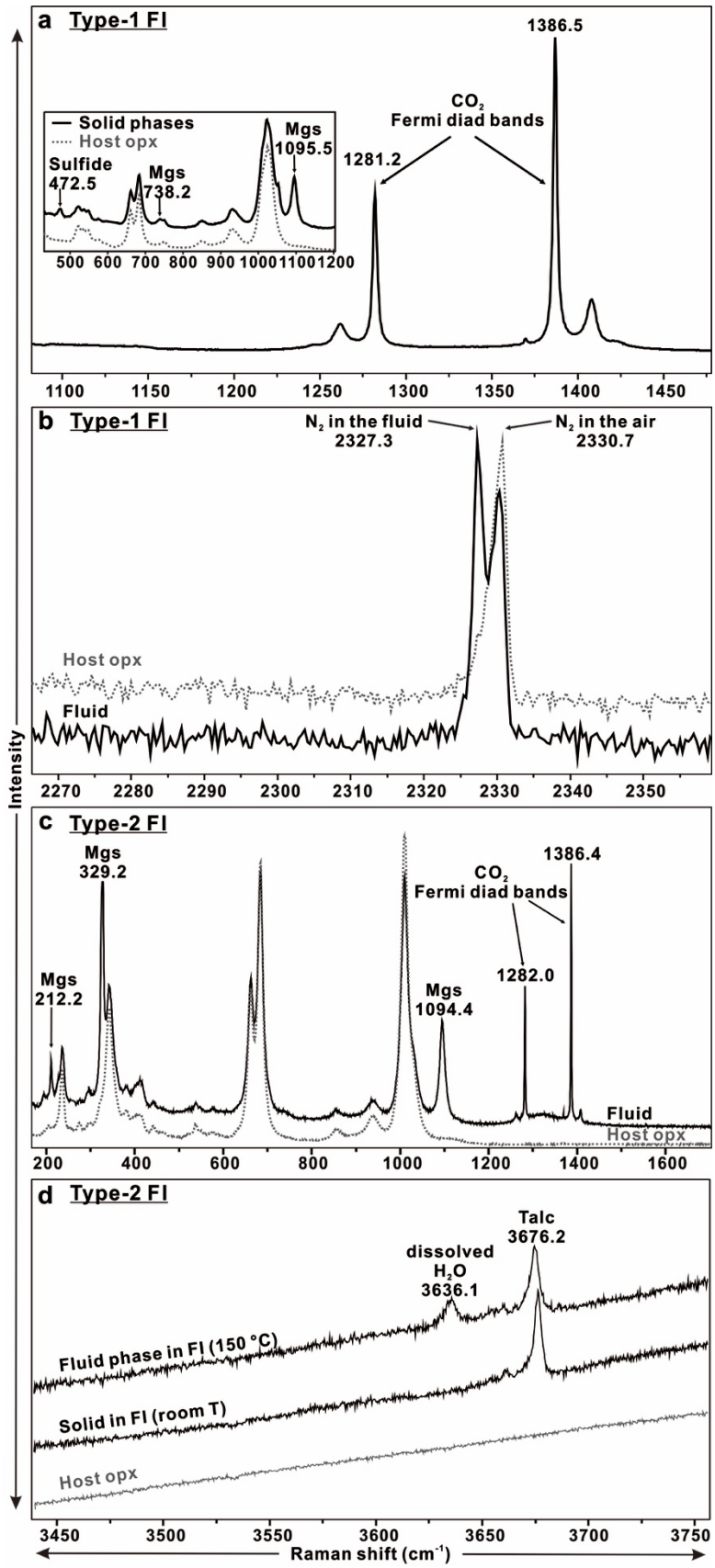
a Type-1 FI
1386.5
CO2
Fermi diad bands
1281.2
Solid phases
Host opx
Sulfide
472.5
Mgs
738.2
Mgs
1095.5
500 600 700 800 900 1000 1100 1200
1100 1150 1200 1250 1300 1350 1400 1450
b Type-1 FI
N2 in the fluid
2327.3
N2 in the air
2330.7
Host opx
Fluid
2270 2280 2290 2300 2310 2320 2330 2340 2350
Intensity
c Type-2 FI
Mgs
329.2
1386.4
CO2
Fermi diad bands
1282.0
Mgs
212.2
Mgs
1094.4
Fluid
Host opx
200 400 600 800 1000 1200 1400 1600
d Type-2 FI
Talc
3676.2
dissolved
H2O
3636.1
Fluid phase in FI (150 °C)
Solid in FI (room T)
Host opx
3450 3500 3550 3600 3650 3700 3750
Raman shift (cm-1)

Fig. 2.4. Representative Raman spectra for orthopyroxene-hosted FIs (a–b: Type-1; c–d: Type-2). (a) Raman spectra for the Fermi diad bands of CO_2 (1281.2 cm^{-1} and 1386.5 cm^{-1}), magnesite (Mgs; 738.2 cm^{-1} and 1095.5 cm^{-1}) and sulfide (472.5 cm^{-1}). (b) Raman spectra for the N_2 peaks between fluid (2327.3 cm^{-1}) and air (2330.7 cm^{-1}). (c) Raman spectra for the Fermi diad bands of CO_2 fluid (1282.0 cm^{-1} and 1386.4 cm^{-1}) and magnesite (Mgs; 1094.4 cm^{-1}). (d) Raman spectra showing the band of dissolved H_2O (3636.1 cm^{-1}) of the fluid phase identified at 150 ºC. In addition, presence of talc has been discovered (band at 3676.2 cm^{-1}) even at room temperature measurements. Grey spectra indicate a reference host spectra off but close to the inclusion applying the same parameters used for the FIs.

2.7. Focused ion beam–scanning electron microscopy (FIB–SEM)

We applied FIB–SEM to observe the morphology and composition of solid phases in unexposed fluid inclusions by using gradational milling steps.

In the Type-1 FIs (n = 6 from xenoliths ADTM18, 27 and 37) (Table 2.2), an opaque phase (Fig. 2.2e) with a size of 1 – 3 μm and having subhedral shape (Fig. 2.5a) appeared in bright contrast compared to the host orthopyroxene in BSE images. EDS analysis indicated that this phase is an Fe (Ni-Cu-Co)-bearing sulfide bleb (Fig. 2.5a and f). Magnesite and quartz, with sizes of 1–1.5 μm and euhedral to subhedral shapes, were also identified (Fig. 2.5a and b). Generally, these minerals from Type-1 FIs directly contact the host orthopyroxene (Fig. 2.5a and b).

Daughter phases from the Type-2 FIs (n = 6 from xenoliths ADTM18, 27 and 37) (Table 2.2) differ from those of the Type-1 FIs and show higher complexity in terms of the solid phases detected. Magnesites with euhedral shape and large size (3–4 μm) (Fig. 2.5c and e) were also found in direct contact with the wall of the host orthopyroxene (Fig. 2.5c–e) relative to the other solid phases within the same fluid inclusion. Moreover, the magnesite is covered by a glass layer (Fig. 2.5e and k), which is similar to the findings of Berkesi *et al.* (2012). There is also a 3 μm size fibrous phase, which is generally attached to magnesite (Fig. 2.5c and d), and is likely the talc also recognized beforehand by micro-Raman analysis (Fig. 2.4d). Additionally, a

1–2 μm subhedral Ca- and S-bearing solid phase was detected. Considering the fact that this phase is dark on the BSE image, we suggest that this phase is a Ca-bearing sulfate, probably anhydrite (Fig. 2.5c and h). In addition, a 2–3 μm subhedral Fe-(Ni)-oxide was also detected (Fig. 2.5c and i) based on its brightness in the BSE image. These two phases, Ca-sulfate and Fe-(Ni)-oxide, appear together on the wall of fluid inclusions (i.e., surface of orthopyroxene) and are covered completely by magnesite (Fig. 2.5c). Within the fluid inclusions of both Type-1 and Type-2 FIs, several vesicles are typically present on the wall of the fluid inclusion and also partly cover the daughter minerals (Fig. 2.5c and d).

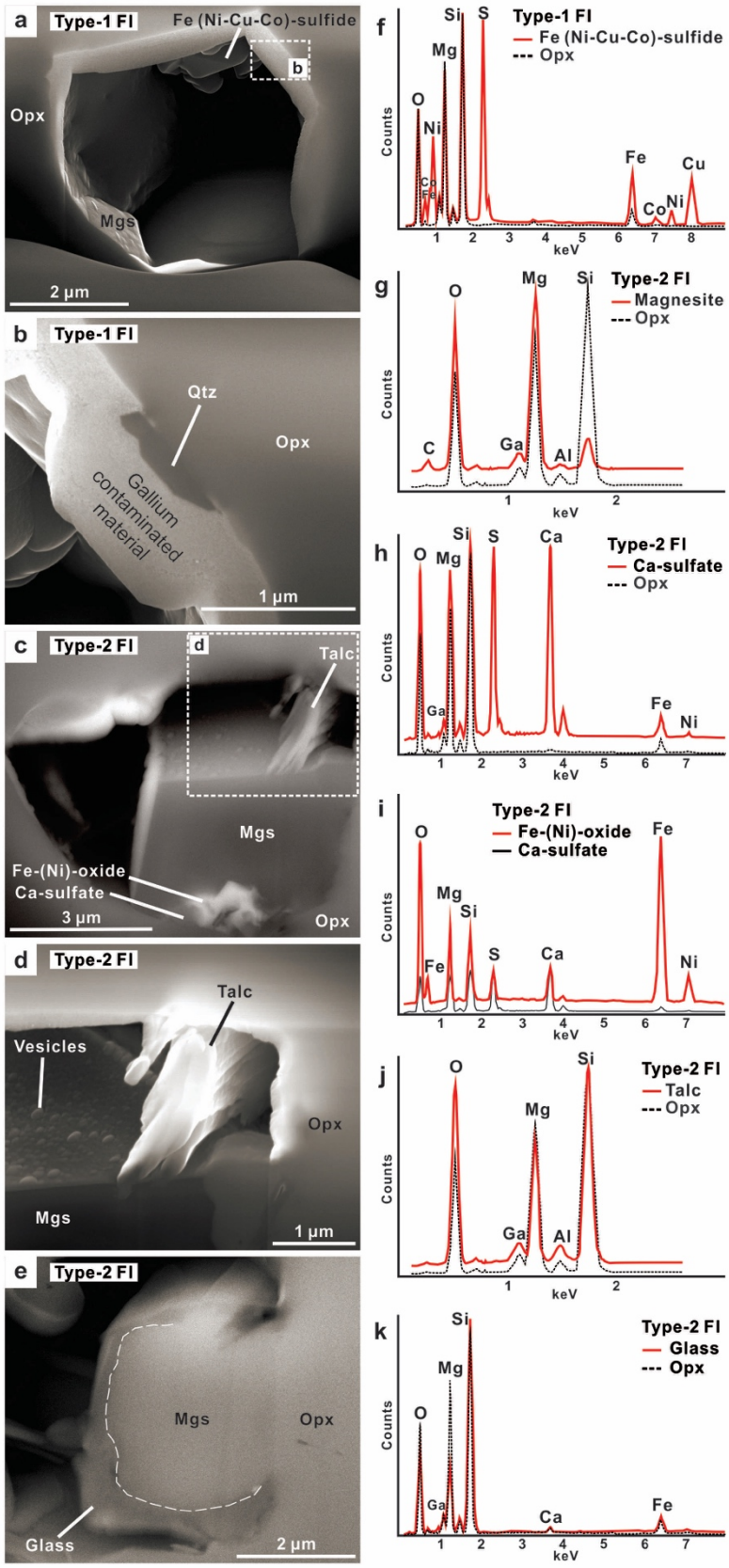
a
Type-1 FI
Fe (Ni-Cu-Co)-sulfide
b
Opx
Mgs
2 µm
b
Type-1 FI
Qtz
Opx
Gallium contaminated material
1 µm
c
Type-2 FI
d
Talc
Mgs
Fe-(Ni)-oxide
Ca-sulfate
3 µm
Opx
d
Type-2 FI
Talc
Vesicles
Opx
Mgs
1 µm
e
Type-2 FI
Mgs
Opx
Glass
2 µm
f
Type-1 FI
Fe (Ni-Cu-Co)-sulfide
Opx
Counts
keV
g
Type-2 FI
Magnesite
Opx
h
Type-2 FI
Ca-sulfate
Opx
i
Type-2 FI
Fe-(Ni)-oxide
Ca-sulfate
j
Type-2 FI
Talc
Opx
k
Type-2 FI
Glass
Opx

Fig. 2.5. Representative images and EDS spectra taken during stepwise FIB exposure of the daughter phases in the Type-1 FI (a–b) and Type-2 FI (c–e) orthopyroxene-hosted fluid inclusions. The secondary electron images of a Type-1 FI (xenolith ADTM27) show (a) Fe (Ni-Cu-Co)-sulfide and magnesite and (b) quartz on the wall of a fluid inclusion. (b) Close-up image from white dashed rectangular area in (a) after milling procedures. (c) Backscattered electron (BSE) image of a Type-2 FI (xenolith ADTM37) showing magnesite, talc, Fe-(Ni)-oxide, and Ca-sulfate. (d) Close-up secondary electron image of talc, magnesite, and glass vesicles on the magnesite from the white dashed square in (c). Talc and magnesite are connected to each other. (e) BSE image of a Type-2 FI (xenolith ADTM18) showing a glass layer on magnesite. (f–k) EDS spectra of daughter and step-daughter phases shown in (a–e).

2.8. Discussion

Both the petrographic features and the fluid inclusion data show the same characters for all the Type-1 and all the Type-2 FIs, irrespectively of their host xenolith (Table 2.3). In the followings, therefore, we discuss our observations and data obtained for Type-1 and Type-2 with no special attention to their enclosing xenolith.

2.8.1. Entrapment of fluid inclusions

A negative crystal shape of fluid inclusions (Fig. 2.2) suggests textural equilibrium between the fluid and its host phase (Roedder, 1984; Viti & Frezzotti, 2000). The development of negative crystal shape through maturation (Bodnar *et al.*, 1989) likely takes a longer period of time than the duration of transport of the xenoliths from the upper mantle to the surface (Roedder, 1984; Szabó & Bodnar, 1996; Dégi *et al.*, 2009). Moreover, the rapid pressure change during uplift does not favor the formation of negative crystal morphology (Bodnar *et al.*, 1989). Thus, the possibility of the entrapment of the studied fluid inclusions by alkali basalt during transport to the surface is highly unlikely.

Although both FI types can be regarded as having been entrapped originally at mantle depth, on the basis of their petrographic features, using the terminology and logic of Roedder (1984) and Van den Kerkhof and Hein (2001), the Type-1 FIs seem to have preserved their original fluid better

because of their high density (between 0.98 and 1.12 g/cm^3; Table 2.3) and the absence of petrographic evidence for significant re-equilibration. In contrast, the Type-2 FIs have CO_2 densities between 0.70 and 0.86 g/cm^3 (Table 2.3) and show strong petrographic evidence for re-equilibration of fluid inclusions to lower densities by partial fluid leakage (Fig. 2.2f). The Type-2 FIs could have decrepitated more easily because they are larger than the Type-1 FIs (2–10 μm for Type-1 and 10–100 μm for Type-2; Table 2.3). A positive correlation between size and the appearance of decrepitation as a result of brittle deformation or stretching as a plastic failure in quartz- and olivine-hosted fluid inclusions has been shown experimentally (Hall & Bodnar, 1989; Wanamaker & Evans, 1989; Yamamoto *et al.*, 2011). The petrography also supports that the studied Type-1 and Type-2 FIs could have been trapped at different times as inclusions of latter type are often crosscutting Type-1 FIs reaching the edge of the host orthopyroxene (Fig. 2.2b). As a consideration, Type-1 FI represents “older” generation fluids entrapped prior to or during the formation of exsolution in the core of orthopyroxene, whereas Type-2 FI represents “younger” generation fluids entrapped after the formation of exsolution lamellae in orthopyroxene porphyroclasts.

2.8.2. Temperature estimate for fluid inclusion entrapment

The occurrence of exsolution lamellae (clinopyroxene and spinel) in the core of orthopyroxene porphyroclasts is a usual phenomenon in the mantle

xenoliths beneath the studied Adam's Diggings (Fig. 2.2a–d). These lamellae are thought to indicate elevated temperatures, possibly resulted to a heating event, followed by a cooling stage during the evolution of the lithospheric mantle (Kil & Wendlandt, 2004). This is the general explanation for such exsolved minerals in mantle xenoliths (e.g., Bedini *et al.*, 1997; Spengler *et al.*, 2012; Pintér *et al.*, 2015) because the steep isopleths of Ca in orthopyroxene (e.g., Gasparik, 2000) require clinopyroxene lamellae and associated Al-mineral phases (in our case spinel) to be formed during cooling (Spengler *et al.*, 2012). However, it has also been suggested based on the study of mantle xenoliths from the Cameroon Volcanic Line (Pintér *et al.*, 2015) that lamellae formation is controlled by the thermal relaxation following extension and thus thinning of the mantle lithosphere. A similar controlling factor is also plausible for the xenoliths studied here, given that the entire lithosphere beneath the Rio Grande Rift preserves a large-scale cooling history, which is partly due to the thermal relaxation of isotherms associated with extension (e.g., Ricketts *et al.* 2016 and references therein).

Exsolution lamellae occur by means of two possible genetic mechanisms: (i) nucleation and growth within the host crystal or (ii) spinodal decomposition (McCallister & Yund, 1977; Putnis, 1992; Sánchez-Muñoz *et al.*, 2016). However, these solid-state mechanisms do not necessarily allow fluid entrapment in the orthopyroxene. We suggest that the entrapment of Type-1 FIs started either before or during the formation of the exsolution lamellae. Type-2 FIs, which are crosscutting the lamellae and Type-1 FIs,

were trapped in their host orthopyroxene after the lamellae were formed.

Following this sequence of events (fluid inclusions and lamellae formation), "paleo" orthopyroxene (before lamellae formation, Opx_{paleo}) compositions were calculated using the vol.% of the lamellae relative to their host orthopyroxene (similar to methods described in Bedini *et al.*, 1997). In the studied orthopyroxene porphyroclasts, the vol.% ranges are: 97-98 ±0.05 vol.% for core of orthopyroxene (where lamellae occur), 1.69-2.37 ±0.05 vol.% for clinopyroxene lamellae, and 0.28-0.52 ±0.05 vol.% for spinel lamellae (Table 2.4). Applying the given vol.%, Opx_{paleo} compositions show a slight increase in Al_2O_3, CaO, Cr_2O_3, and Na_2O (Table 2.4). Owing to the lack of known clinopyroxene composition before lamellae formation, it was not possible to apply a two-pyroxene thermometer. Instead, the Ca-in-opx thermometers developed by Brey and Köhler (1990) and Nimis and Grütter (2010), were applied, both set at 1.5 GPa. As a result, "paleo" temperatures (before exsolution of clinopyroxene and spinel, T_{paleo}) as well as "neo" temperatures (after exsolution of clinopyroxene and spinel, T_{neo}) were calculated (Table 2.4). T_{paleo} varies between 1056–1094 (±16 °C) using the method of Brey and Köhler (1990) and between 1051–1093 (± 25 °C) using the method of Nimis and Grütter (2010). Values of T_{neo} show lower temperatures of 952–969 (±16 °C) using the method of Brey and Köhler (1990) and 931–951 (± 25 °C) using the method of Nimis and Grütter (2010). As a consequence, minimum temperature conditions for Type-1 FI entrapment are determined by T_{neo} and can also be explained at even higher

temperatures than T_{paleo}. Entrapment temperature for Type-2 can rather be estimated to fall between T_{neo} and the equilibrium temperatures of the xenoliths (the latter temperatures are already published by Kil & Wendtland, 2004) that gives a temperature interval between 870 and 980 (±16 °C).

Table 2.4. Representative electron microprobe data with calculated paleo and neo temperatures in the studied samples.

Sample	ADTM07				ADTM13				ADTM18				ADTM27				ADTM37			
vol%	Opx_{97} $Cpx_{2.18}$ $Sp_{0.52}$				Opx_{97} $Cpx_{2.25}$ $Sp_{0.29}$				Opx_{98} $Cpx_{1.69}$ $Sp_{0.28}$				Opx_{98} $Cpx_{1.77}$ $Sp_{0.32}$				Opx_{97} $Cpx_{2.37}$ $Sp_{0.41}$			
Mineral	Opx	Sp	Cpx	Opx^{paleo}	Opx	Sp	Cpx	Opx^{paleo}	Opx	Sp	Cpx	Opx^{paleo}	Opx	Sp	Cpx	Opx^{paleo}	Opx	Sp	Cpx	Opx^{paleo}
SiO_2	56.54	0.07	53.20	56.18	55.06	0.09	52.13	54.84	55.87	0.06	52.49	55.57	55.13	0.09	52.38	54.91	56.41	0.06	53.48	56.11
TiO_2	0.06	0.13	0.12	0.06	0.04	0.07	0.18	0.05	0.01	0.11	0.21	0.01	0.03	0.03	0.11	0.03	0.07	0.11	0.11	0.07
Al_2O_3	1.94	26.88	3.38	2.10	3.45	46.23	4.65	3.60	3.20	26.95	5.17	3.29	3.54	48.77	4.97	3.71	2.00	26.99	3.36	2.14
Cr_2O_3	0.39	37.94	1.24	0.60	0.48	18.65	1.02	0.54	0.33	39.50	1.05	0.45	0.41	16.69	0.75	0.47	0.49	39.67	1.38	0.67
FeO	5.72	17.13	3.05	5.72	6.96	15.36	3.62	6.91	7.15	16.36	3.30	7.09	6.78	13.14	3.51	6.74	5.34	16.91	2.89	5.33
MnO	0.16	0.24	0.09	0.16	0.12	0.15	0.11	0.12	0.15	0.22	0.12	0.14	0.19	0.16	0.09	0.19	0.15	0.23	0.04	0.15
MgO	33.87	16.49	16.20	33.40	32.53	17.87	15.43	32.10	32.41	15.98	14.99	32.02	32.25	19.81	15.49	31.92	33.94	15.62	15.86	33.43
CaO	0.70	0.02	21.04	1.14	0.68	0.01	21.14	1.14	0.68	0.00	20.43	1.01	0.65	0.02	20.63	1.00	0.67	0.01	21.32	1.16
Na_2O	0.07	0.04	1.62	0.10	0.02	0.02	1.25	0.05	0.00	0.00	1.46	0.03	0.10	0.10	1.39	0.13	0.12	0.00	1.54	0.15
K_2O	0.00	0.00	0.00	0.00	0.00	0.03	0.00	0.00	0.01	0.00	0.00	0.01	0.02	0.00	0.02	0.02	0.01	0.00	0.00	0.01
NiO	0.11	0.24	0.03	0.11	0.09	0.31	0.03	0.09	0.10	0.17	0.06	0.09	0.07	0.30	0.04	0.07	0.03	0.17	0.03	0.03
Total	99.56	99.18	99.96	99.57	99.44	98.80	99.54	99.44	99.90	99.35	99.28	99.72	99.16	99.09	99.38	99.16	99.23	99.75	100.00	99.25
	T_{neo}	T_{paleo}		$_{delta}T$	T_{neo}	T_{paleo}		$_{delta}T$	T_{neo}	T_{paleo}		$_{delta}T$	T_{neo}	T_{paleo}		$_{delta}T$	T_{neo}	T_{paleo}		$_{delta}T$
$B\&K_{1990}$	969	1090	± 16°C	121	963	1091	± 16°C	128	964	1059	± 16°C	96	952	1056	± 16°C	104	959	1094	± 16°C	136
$N\&G_{2010}$	951	1089	± 25°C	138	944	1089	± 25°C	146	944	1055	± 25°C	110	931	1051	± 25°C	121	939	1093	± 25°C	154

Opx: orthopyroxene; Sp: spinel; Cpx: clinopyroxene; Opx^{paleo}: paleo orthopyroxene; vol%: volume% between orthopyroxene, clinopyroxene, and spinel; T_{neo}: neo temperatures (after the lamellae formation); T_{paleo}: paleo temperature (prior to the formation of the lamellae); $_{delta}T$: The difference between neo and paleo temperatures; $B\&K_{1990}$: Ca-in-opx thermometer by Brey & Köhler (1990); $N\&G_{2010}$: modified calculation by Nimis & Grütter (2010).

2.8.3. Type-1 FIs

Fluids in the Type-1 FIs likely contain small amounts of N_2 (because of their low-intensity peak on the Raman spectrum, Fig. 2.4b) that can be responsible for the melting point depression of the T_m (van den Kerkhof, 1988). High density fluid inclusions CO_2 is common in mantle fluids (Frezzotti *et al.*, 2002; Berkesi *et al.*, 2009; Frezzotti *et al.*, 2010; Berkesi *et al.*, 2012; Frezzotti *et al.*, 2012a) and N_2 may also be a minor but a common component in subcontinental lithospheric upper-mantle fluids (Berkesi et al., 2016). According to Frost & McCammon (2008), at spinel lherzolite stability, the oxygen fugacity is within ± 2 log units of the fayalite–magnetite–quartz (FMQ) buffer, which results in only the presence of N as N_2 (and H_2O) in the H–N–O system (Watenphul et al., 2010). In general, the redox condition provides the main control on the liberation of N_2 from the convecting mantle (Smith et al., 2014) by the oxidation of NH^{4+} in hydrous silicates (mostly phlogopite) to mobile N_2. Based on previous petrographic observations (Kil & Wendtland, 2004), phlogopite is present in the ADTM xenoliths (ADTM 18, 27, 37, Table 2.1) that can be regarded as potential sources of nitrogen that could have been liberated due to the precedent heating event, possibly as a consequence of lithosphere attenuation during early rifting as already assumed by Kil & Wendtland (2004). In this scenario, H_2O is also expected in the fluid phase. It is important to emphasize that the previous existence of H_2O cannot be excluded even though Type-1 FIs were found to be water-free through diffusive loss via nano-cracks (e.g., Viti & Frezzotti, 2000) and even

though the petrographic features of the inclusion do not show any visible signs of re-equilibration. This point, however, must be better investigated and clarified by further investigation.

2.8.4. Type-2 FIs

As mentioned before, the Type-2 event represents a later stage fluid invasion that was trapped after the formation of lamellae in the orthopyroxene porphyroclasts. In contrast to the Type-1 FI, Type-2 FIs are H_2O-bearing and contain numerous phases (Fig. 2.5c) such as silicate glass film (Fig. 2.5e) covering the magnesite, talc, Ca-sulfate (likely anhydrite), and Fe-Ni oxide. The presence of talc and sulfate is in good accord with the interpretation of this being a common feature in CO_2–H_2O fluid by Frezzotti *et al.* (2010), also arguing that such types of fluids may be widespread in the upper mantle, even in extensional setting.

Silicate glass film in mantle fluid inclusions from the Central Pannonian Basin was previously reported by Berkesi *et al.* (2012), who concluded that silicate melt components were dissolved in the H_2O-bearing CO_2-rich fluid at entrapment. Moreover, various trace elements, inheriting the characteristics of the parental melt, are considered to be dissolved in H_2O-bearing CO_2-rich fluid at high pressure and temperature that formed via silicate (andesitic) melt/volatile immiscibility (Szabó *et al.*, 2009; Hidas *et al.*, 2010). It has also been suggested that, following this phase separation, melt and fluid evolved along different paths and therefore could have migrated

separately at upper mantle depth, interacting with the peridotitic rocks. We suppose that Type-2 FIs may originate from such processes, where only the separated fluid phase was trapped in the studied rocks. During cooling, probably after eruption of the basaltic host, the minor amount of dissolved silicate melt quenched onto the wall of the inclusion as proposed by Hidas *et al.* (2010).

2.8.5. Possible source of the fluids related to metasomatic evolution in the Adam's Diggings

Previous petrological and major & trace element data on the mantle xenoliths' constituent minerals indicated three metasomatic events beneath ADTM (referred to as MM1, MM2, and MM3, following Kil & Wendlandt, 2007). The timing of MM1 (the first enrichment process) is thought to be related to prior to rifting (older than 37 Ma) when the upper mantle beneath the Rio Grande Rift was heterogeneous with MORB- and OIB-type (old subducted slab) mantle components (Frey & Prinz, 1978; Kyser & Rison, 1982; Leeman, 1982; Roden *et al.*, 1988). The MM1 may have been recorded by a K^+-enriched fluid/melt originated from an old subducted slab (the Farallon plate) and likely precipitated a hydrous mineral (i.e., phlogopite) (Kil & Wendlandt, 2007). This is consistent with the hydration process related to the flat subduction of the Farallon slab (until 40 Ma) in western North America (Smith *et al.*, 1999; Smith, 2000; Lee, 2005). At this state, however, the porphyroclastic texture did not likely develop (Fig. 2.6a). Regarding our

observation that inclusions are hosted in orthopyroxene porphyroclasts, we suppose that the MM1 metasomatic process was an earlier event than the entrapment of both fluid inclusion types (Fig. 2.6).

There were two magmatic pulses in the RGR related to early rifting between 37–15 Ma and late rifting between 15–0 Ma (Baldridge *et al.*, 1980). These magmatic pulses are closely associated with two metasomatic events beneath the Adam's Diggings (Fig. 2.6): MM2, which was triggered by dehydration melting of hydrous minerals (possibly phlogopite), whereas MM3 involved infiltration of the host alkali basaltic-basanitic melt or melt with similar composition (Kil & Wendlandt, 2007). During early rifting with a magmatic pulse (heating; MM2 metasomatic event), deformation (porphyroclastic) textures were developed; as a result, pressure and temperature conditions were changed in the thinning lithosphere (Kil & Wendlandt, 2007; Park *et al.*, 2014). This is also represented by exsolution lamellae of clinopyroxene and spinel in orthopyroxenes (Fig. 2.2a–d).

Probably after the MM2 and deformation process, Type-1 FI (CO_2-N_2) may have been trapped before or during formation of exsolution lamellae (Fig. 2.6b). This is not likely to be a potential source of any metasomatic processes because there is no evidence for H_2O, silicate melt, or chlorine that are all known to be capable of dissolving and transporting trace elements at mantle depth (*e.g.*, O'Reilly & Griffin, 2012).

In contrast to Type-1 FI, Type-2 FI can be regarded as a potential source of metasomatic processes because Type-2 FI contains both H_2O and

silicate glass (formerly dissolved melt component, Fig. 2.5e) possibly representing the fluid-rich part of a precedent silicate melt/fluid immiscibility (see section 8.4.). After the cooling process, enhanced by early magmatism associated with tectonic extension (early rifting), MM3 metasomatism was recorded (Kil & Wendlandt, 2007; Park *et al.*, 2014). Therefore, during the MM3 metasomatism, COHS-rich fluid could have been liberated through melt/fluid immiscibility and trapped as Type-2 FI (Fig. 2.6c).

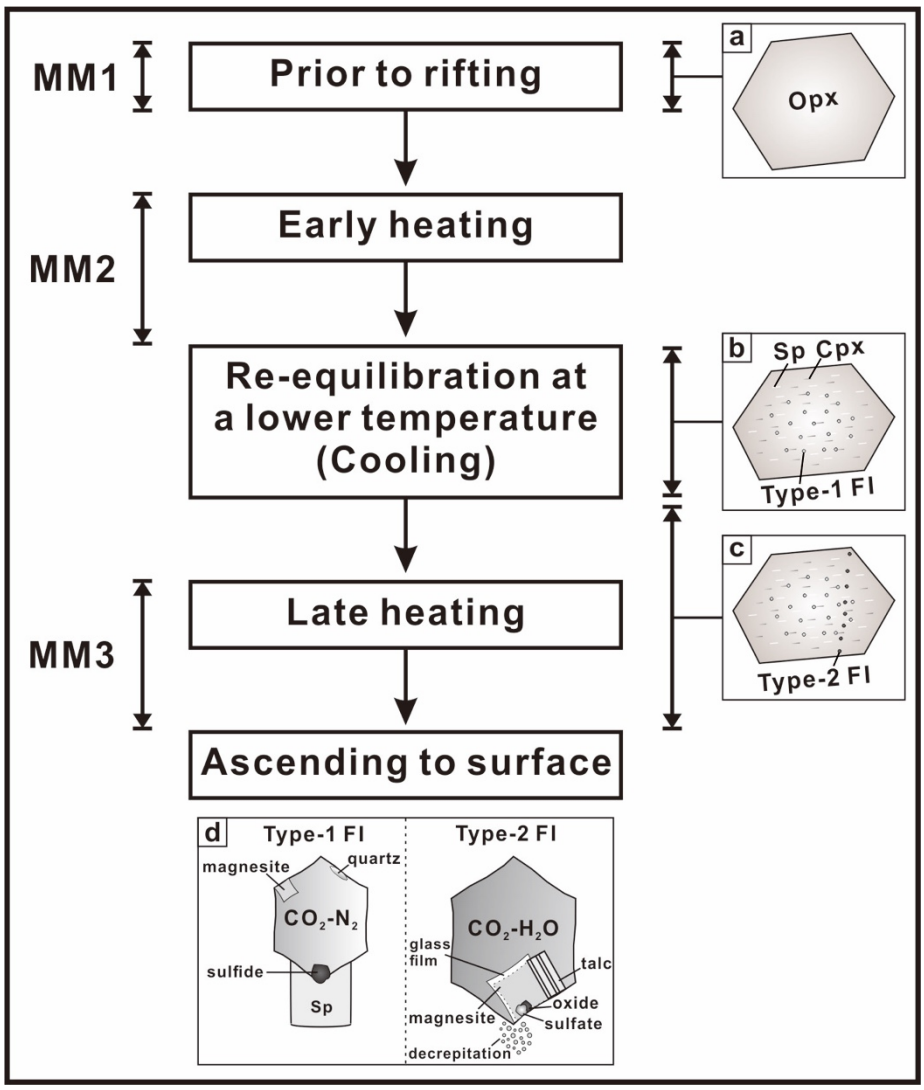

Fig. 2.6. Possible scenario of fluid invasions related to metasomatic events and thermal history beneath the Adam's Diggings. (a) Protogranular (non-deformed) orthopyroxene grain which has experienced MM1 event prior to rifting. (b) After MM2 and possibly simultaneous deformation process (Kil & Wendlandt, 2004; Park *et al.*, 2014), Type-1 FI entrapped before or during formation of exsolution lamellae (induced by cooling). (c) After cooling process, Type-2 FI was trapped related to MM3 event. (d) schematic draw of

room temperature phase relations of both FI generations (Type-1 & 2). MM1 to MM3: three mantle metasomatic events in the Adam's Diggings (Kil & Wendlandt, 2007); Opx: orthopyroxene; Sp: spinel lamellae; Cpx: clinopyroxene lamellae; FI: fluid inclusion. For details, see text.

2.8.6. Post-entrapment reaction processes within inclusions

Magnesite and quartz in the Type-1 FIs (Fig. 2.5a and b) but Mg-carbonate and talc in the Type-2 FIs (Fig. 2.5c and d) were observed only within the inclusions in the studied xenoliths. Therefore, these solids may likely be considered to be "step-daughter crystals" (Scambelluri & Philippot, 2001) originated from a post-entrapment carbonation reaction between the trapped CO_2-rich fluid and the host orthopyroxene (Berkesi *et al.*, 2012; Frezzotti *et al.*, 2012a) by one of the two following reactions, respectively:

$$MgSiO_3 \text{ (orthopyroxene)} + CO_2 \text{ (fluid)} = MgCO_3 \text{ (magnesite)} + SiO_2 \text{ (quartz)} \quad (1)$$

$$4MgSiO_3 \text{ (orthopyroxene)} + CO_2 \text{ (fluid)} + H_2O \text{ (fluid)} = Mg_3Si_4O_{10}(OH)_2 \text{ (talc)} + MgCO_3 \text{ (magnesite)} \quad (2)$$

When comparing the reactions in Eq. (1) and Eq. (2), it can be stated that the amount of H_2O must be somehow different between the two reactions because the reaction products in Eq. (1) are nominally anhydrous whereas one reaction product in Eq. (2) contains H_2O (i.e., talc). Thus, we can conclude that in case of the Type-2 FIs the amount of H_2O within the fluid inclusion was high enough to form talc instead of quartz. The reaction of Eq. (1) may have commenced at a temperatures significantly lower than the mantle condition described on the basis of mantle fluid inclusions from the Central Pannonian Basin by Berkesi *et al.* (2012). The reactions of Eq. (1) and (2) within the

fluid inclusions could have begun where the CO_2 isochors intersect the carbonation reaction curve(s). To reveal the possible P–T conditions for the reaction in Eq. (1), thermodynamic modeling using Perple_X 6.8.8 software (Connolly, 2009) was carried out in a manner similar to that described in Berkesi *et al.* (2012). Eq. (2) was also examined by similar thermodynamic modeling. In the $MgO–SiO_2–CO_2–H_2O$ system, the Schreinemakers projection was used to create a pressure–temperature plane excluding all phases, except for enstatite, magnesite, talc, and the $CO_2–H_2O$ fluid mixture. In Fig. 2.7, we did not take into account the reaction curves for H_2O-dominant fluids, but rather considered only CO_2-rich ones because the fluid in studied xenoliths showed CO_2-dominance. This reaction curve shows that the commencement temperature for magnesite and quartz in the Type-1 FIs should be 520–630 °C (gray area in Fig. 2.7a), whereas the temperature for talc and magnesite formation in the Type-2 FIs should be 520–610 °C (shaded area in Fig. 2.7b). The temperatures exclude the possibility that the reactions of Eqs. (1) and (2) took place at mantle conditions.

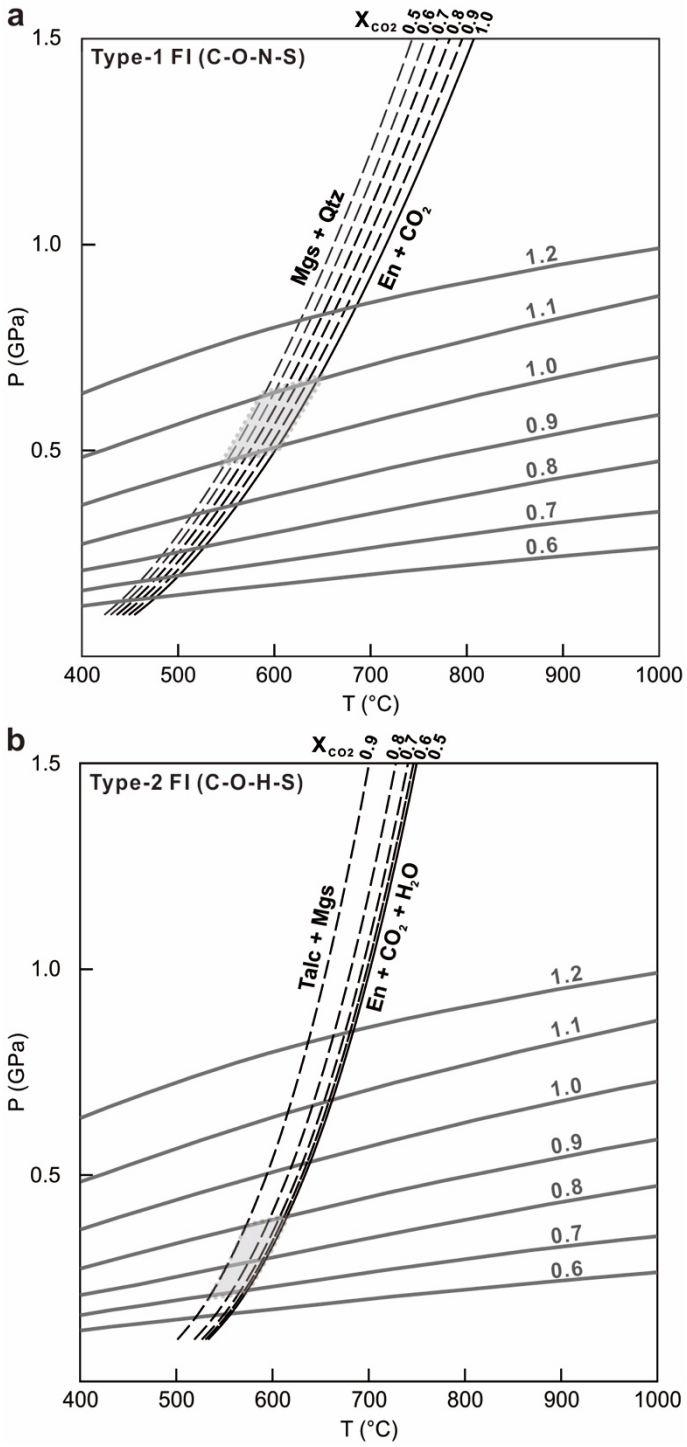

Fig. 2.7. Pressure (GPa)−Temperature (°C) diagram showing the inferred formation conditions of step-daughter minerals. (a) For the Type-1 FIs, the

reaction curves of enstatite (En) + CO_2 = magnesite (Mgs) + quartz (Qtz) are shown in black solid and dashed lines. (b) For the Type-2 FIs, the reaction curves of enstatite (En) + CO_2 + H_2O = magnesite (Mgs) + talc are shown in black solid and dashed lines. The gray solid lines with numbers (0.6−1.2) in (a–b) correspond to the isochores of CO_2 labeled in g/cm^3. The shaded areas in (a–b) indicate the possible temperature range within which the carbonation reaction could have started.

2.9. Conclusions

Fluid inclusions trapped in orthopyroxene porphyroclasts in spinel peridotite xenoliths from the rift shoulder of the Rio Grande Rift, namely from Adam's Diggings, were the subject of this study. Petrography, microthermometry, Raman microspectroscopy, and the FIB–SEM technique were used to describe two generations of fluid inclusions (Type-1 and Type-2). Results indicate at least two fluid invasions beneath the western margin of RGR mantle with different fluid compositions and at time of entrapment.

Type-1 FIs (C–O–N–S) in orthopyroxenes were trapped from the earlier fluid invasion before or during a cooling event, that is evidenced by the presence of clinopyroxene and spinel lamellae exsolved from high-temperature orthopyroxene porphyroclasts. Type-2 FIs (C–O–H–S) entrapped following the formation of the lamellae in orthopyroxene representing a later stage fluid invasion. These two fluid invasions in the upper mantle beneath Adam's Diggings indicate the complexity of mantle fluids in the RGR. During the post-eruption cooling of the xenoliths enclosed in the host alkali basaltic melt, post-entrapment reactions within the inclusions produced magnesite and quartz in Type-1 FIs and magnesite and talc in Type-2 FIs as reaction products of the fluid and its host mineral (orthopyroxene).

CHAPTER 3

Microstructural evolution of the Yugu peridotites in the Gyeonggi Massif, Korea: Implications for olivine fabric transition in mantle shear zones

Abstract

Large-scale emplaced peridotite bodies may provide insights into plastic deformation process and tectonic evolution in the mantle shear zone. Due to the complexity of deformation microstructures and processes in natural mantle rocks, the evolution of pre-existing olivine fabrics is still not well understood. In this study, we examine well-preserved transitional characteristics of microstructures and olivine fabrics developed in a mantle shear zone from the Yugu peridotite body, the Gyeonggi Massif, Korean Peninsula. The Yugu peridotite body predominantly comprises spinel harzburgite together with minor lherzolite, dunite, and clinopyroxenite. We classified highly deformed peridotites into four textural types based on their microstructural characteristics: proto-mylonite; proto-mylonite to mylonite transition; mylonite; and ultra-mylonite. Olivine fabrics changed from A-type (proto-mylonite) via D-type (mylonite) to E-type (ultra-mylonite). Olivine fabric transition is interpreted as occurring under hydrous conditions at low temperature and high strain, because of characteristics such as Ti-clinohumite

defects (and serpentine) and fluid inclusion trails in olivine, and a hydrous mineral (pargasite) in the matrix, especially in the ultra-mylonitic peridotites. Even though the ultra-mylonitic peridotites contained extremely small (24−30 μm) olivine neoblasts, the olivine fabrics showed a distinct (E-type) pattern, which is a unique feature, rather than a random one. Analysis of the lattice preferred orientation strength, dislocation microstructures, and grain size of olivine suggest that proto-mylonitic peridotites were deformed by dislocation creep, whereas both mylonitic and ultra-mylonitic peridotites were deformed by dislocation accommodated grain boundary sliding.

Keywords: olivine fabric transition, mantle shear zone, deformation mechanism, water, Yugu peridotite

3.1. Introduction

Compared to small-scale mantle xenoliths, large-scale emplaced peridotite bodies provide greater insights into petrological, geochemical, geophysical and tectonic evolution in the mantle (e.g., partial melting, melt–rock reaction, and plastic deformation) (Bodinier & Godard, 2003). Ophiolitic and orogenic peridotites often display a ductile shear zone where localized deformation occurs at a variety of length scales. As the mantle shear zone plays a crucial role in large-scale tectonic evolution, and even plate tectonics, understanding the factors that control the initiation and development of shear localization is crucial.

Over the past decade, a large number of studies have been conducted to understand the development of natural mantle shear zones (Handy, 1989; Drury *et al.*, 1991; Furusho & Kanagawa, 1999; Dijkstra *et al.*, 2002; Michibayashi & Mainprice, 2004; Precigout *et al.*, 2007; Skemer *et al.*, 2010; Kaczmarek & Tommasi, 2011; Linckens *et al.*, 2011; Hidas *et al.*, 2013; Jung *et al.*, 2014; Herwegh *et al.*, 2016). In general, shear localization has been attributed to grain size reduction promoted by the fluxing of a reactive melt (Dijkstra *et al.*, 2002), metamorphic reactions (Newman *et al.*, 1999), deformation-induced dynamic recrystallization (Drury *et al.*, 1991), and cataclasis (Vissers *et al.*, 1997). However, many of these scenarios are not well-constrained (Skemer *et al.*, 2013).

Information on mechanical properties of the lithosphere and the

relative strength of the crust and upper mantle is essential in order to understand geodynamic processes. Lithosphere rheology varies significantly, depending on a range of physicochemical parameters, such as temperature, pressure, mineral assemblage, grain size, melt/fluid content and composition, and differential stress conditions (Bürgmann & Dresen, 2008). Incorporation of water in minerals and the presence of melt can dramatically reduce the strength of mantle rocks (Mackwell *et al.*, 1985; Karato *et al.*, 1986; Hirth & Kohlstedt, 1995; Mei *et al.*, 2002; Karato & Jung, 2003; Zimmerman & Kohlstedt, 2004), and also influence deformation microstructures and processes (Dijkstra *et al.*, 2004; Skemer *et al.*, 2010; Soustelle *et al.*, 2010; Kaczmarek & Tommasi, 2011; Jung *et al.*, 2014; Linckens *et al.*, 2015). Previous experimental studies have shown that olivine fabric is controlled by stress, temperature, and water content (Jung & Karato, 2001a; Katayama *et al.*, 2004; Jung *et al.*, 2006; Katayama & Karato, 2006). However, the evolution of pre-existing olivine fabrics in natural mantle shear zones is not well understood. In this study, we conducted a detailed analysis of microstructures and petrofabrics in the Yugu peridotites from the Gyeonggi Massif (Korean Peninsula) in order to understand the development of olivine fabric in a natural mantle shear zone.

3.2. Geologic setting

The Korean Peninsula consists of three major Precambrian massifs (the Nangrim, Gyeonggi, and Yeongnam) juxtaposed along two Neoproterozoic–Paleozoic fold-thrust belts, the Imjingang and Ogcheon (Cho *et al.*, 2013) (Fig. 3.1a). Ultramafic bodies are sparsely distributed in the southwestern part of the Gyeonggi Massif. The Gyeonggi Massif has been considered as a possible eastward extension area of the Chinese collision belt (Qinling–Dabie–Sulu HP/UHP terrane) between the Sino-Korean (North China) and Yangtze (South China) blocks (Oh *et al.*, 2005; Kim *et al.*, 2006; Oh & Kusky, 2007; Kwon *et al.*, 2009), but this is still debated (Ree *et al.*, 1996; Chough *et al.*, 2000; Cho *et al.*, 2007; Cho *et al.*, 2013; Choi, 2014).

The Gyeonggi Massif consists mainly of Precambrian metamorphic rocks and Mesozoic granitoids (Lee *et al.*, 2003), with two peridotite-dominated areas in the southwestern part of the massif at Hongseong and Yugu. In the Hongseong area, isolated and lenticular-shaped small ultramafic bodies (< 1 km) occur as highly serpentinized dunite and harzburgite (Oh *et al.*, 2012), which are generally distributed in a NNE trend, parallel to the main NNE fault orientation (Seo *et al.*, 2013). The Yugu peridotite body (2 x 4 km) (Fig. 3.1a and b) is considered as an orogenic massif and is one of the largest ultramafic bodies in Korea (Cho & Kim, 2005). The body is emplaced into the Precambrian Yugu granitic gneiss (Fig. 3.1b), and it consists of biotite, amphibole, garnet, sillimanite, muscovite, plagioclase, and quartz (Kim *et al.*,

2003). The age of Yugu granitic gneiss was reported as 1863 Ma, based on sensitive high mass-resolution ion microprobe (SHRIMP) zircon age (Kim *et al.*, 2006). However, lithotectonic boundaries between the ultramafic body and basement rock are poorly constrained in the absence of geochronological and structural data. Despite its tectonic and rheological importance, only a few mineralogical and petrological studies on the Yugu peridotite body have been published to date (Woo & Cho, 2002; Cho & Kim, 2005; Arai *et al.*, 2008). Arai *et al.* (2008) reported amphibole-bearing spinel lherzolites showing mylonitic to strongly porphyroclastic textures, with estimated equilibrium temperatures (two-pyroxene thermometer) of about 1000 °C and 800 °C from porphyroclasts and neoblasts, respectively. Their interpretation was that the Yugu peridotites had a similar petrogenetic setting as sub-arc or abyssal peridotites, and experienced successive cooling with hydration from upper mantle to crustal conditions.

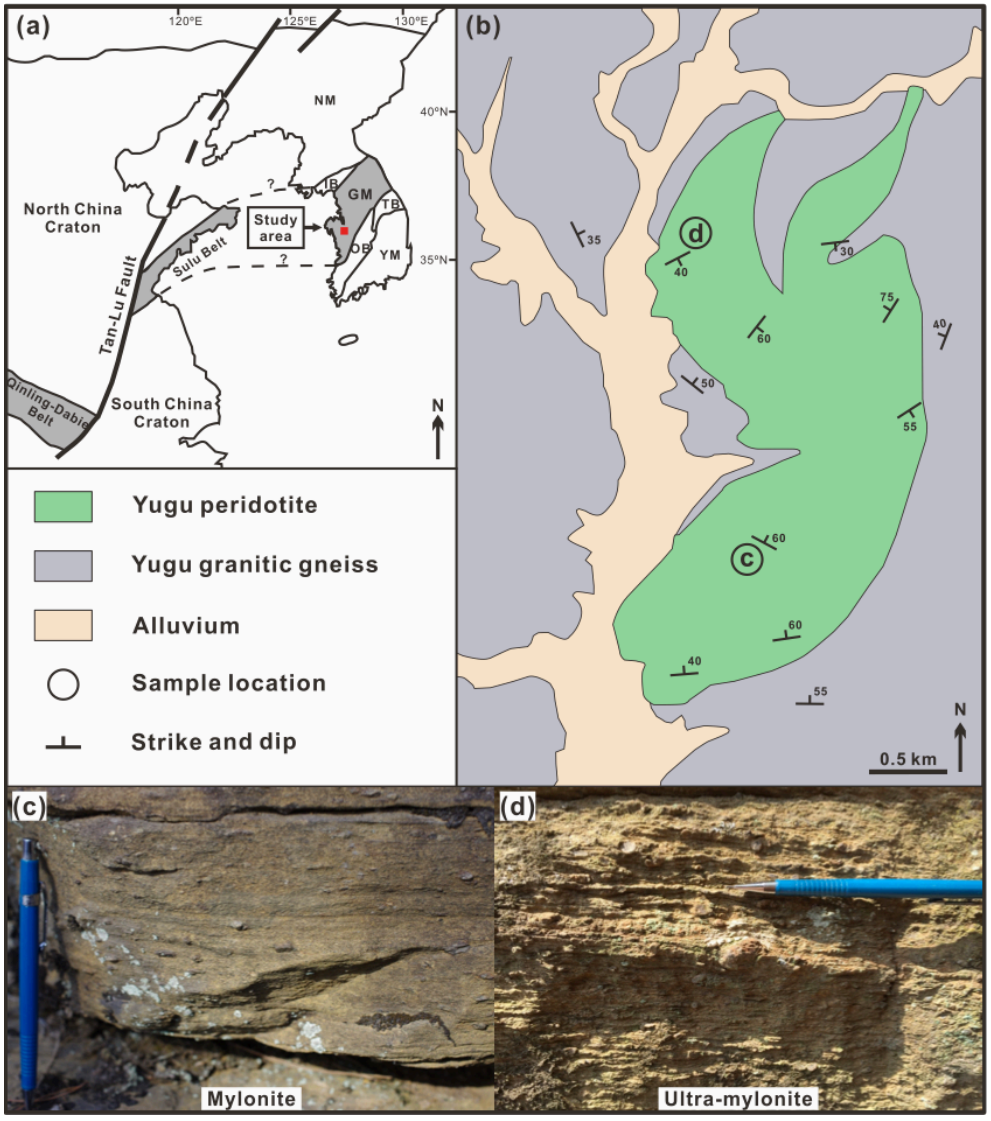

Fig. 3.1. (a) Simplified tectonic map of Northeast Asia showing location of the study area at Yugu in South Korea. NM (Nangrim Massif), IB (Imjingang Belt), GM (Gyeonggi Massif), TB (Taebaeksan Basin), OB (Okcheon Belt), and YM (Yeongnam Massif). (b) Geologic map of the Yugu peridotite in the southwestern Gyeonggi Massif, South Korea. Modified after 1:50,000 geological map from the Korea Institute of Geoscience and Mineral Resources (KIGAM). (c, d) Representative peridotites from the study area shown in (b).

3.3. Field observations and sampling

Field observation showed that the strike (dip) of basement rock varied between N80E and N30W (70NW and 60NE). The peridotite body is normally overlain by granitic gneiss with foliation sub-parallel to the contact (Fig. 3.1b), and the contact areas are often reactivated by small brittle faults accompanied by strong serpentinization. The relatively fresh part of peridotite body shows lateral and vertical extension of several meters. The Yugu peridotite body predominantly comprises spinel harzburgite together with minor lherzolite, dunite, and pyroxenite, and the majority is significantly serpentinized.

We collected fresh samples from two areas (northwestern and southwestern) (Fig. 3.1b and Table 3.1), although we were not able to map the detailed structure and lithology owing to alteration and lack of exposures. The strike (dip) of the southwestern (SW) and northwestern (NW) areas of the peridotites were N60W (60NE) and N60E (60SE), respectively. The NW is located nearer to serpentinite and adjacent migmatitic gneisses (basement rock) than the SW (Fig. 3.1b). Peridotites from the SW area showed proto-mylonitic or mylonitic textures (Fig. 3.1c), whereas those from the NW area displayed ultra-mylonitic texture (Fig. 3.1d). The matrix grain size of the former was larger than the latter. Even though both peridotites showed well-developed foliation with compositional layering, pyroxenite layers were much more common in the NW area (Fig. 3.1d). Compositional layers were

generally parallel (or sub-parallel) to the foliations. Orthopyroxene and spinel porphyroclasts were strongly elongated in the NW area, and generally showed flattening structures.

Table 3.1. Sample descriptions and results of the studied Yugu peridotites.

Sample	Area	Rock	Texture[a]	Modal composition (%)					Ol LPO type	Fabric strength		Max. Aspect ratio (Opx x:z)	Ol grain-size (μm)[b]	Stress (MPa)		
				Ol	Opx	Cpx	Sp	Amp		M-index	J-index			Karato et al. (1980)	Van der Wal et al. (1993)	J & K (2001b) wet
YG-4	SW	Sp-Hzb	PM	83	13	1	3	tr	A	0.19	4.50	5:1	621	9	11	
YG-7P	SW	Sp-Hzb	PM	85	12	0	3	tr	A	0.10	2.75		530	10	12	
YG-7M	SW	Sp-Hzb	M	75	17	2	4	2	D	0.06	2.34	10:1	322	15	18	
YG-8	SW	Sp-Hzb	M	77	15	2	4	2	D	0.07	2.64		281	17	20	
YG-9	NW	Sp-Lhz	UM	69	18	6	3	4	E	0.05	2.08	50:1	30	116	108	280
YG-10	NW	Sp-Lhz	UM	67	17	7	4	5	E	0.02	1.60		24	141	127	310

The southwestern (SW) and northwestern (NW) areas of the Yugu peridotites. Hzb: harzburgite, Lhz: lherzolite, Ol: olivine, Opx: orthopyroxene, Cpx: clinopyroxene, Sp: spinel, Amp: amphibole, tr: trace, and J & K: Jung and Karato.

[a] PM: proto-mylonite, M: mylonite, UM: ultra-mylonite.

[b] Mean grain-size (3D) of olivine in the matrix.

3.4. Microstructures

High-quality thin sections, oriented perpendicular to the foliation and parallel to the lineation (i.e., XZ plane), were taken for microstructural observation and analysis. Foliation was determined by alignment of spinel and pyroxene porphyroclasts with compositional layering of pyroxenes. Lineation was determined by using shape preferred orientation (SPO) of olivine, pyroxene, and spinel in the foliation.

The samples were all spinel peridotites consisting of olivine, orthopyroxene, clinopyroxene, spinel, and amphibole (Table 3.1). Based on microstructural characteristics of highly deformed peridotites (especially olivine grain size), we classified them into four textural types: proto-mylonite (Fig. 3.2a); proto-mylonite to mylonite transition (Fig. 3.2b); mylonite (Fig. 3.2c); and ultra-mylonite (Fig. 3.2d). Clinopyroxene and hydrous mineral (i.e., amphibole) content generally increased from the proto-mylonite (harzburgite) via mylonite (harzburgite) to ultra-mylonite (lherzolite), and also from the SW area to the NW (Table 3.1).

Proto-mylonitic peridotite (harzburgite; YG-4) consisted of olivine, orthopyroxene, spinel, and minor clinopyroxene and amphibole, and was characterized by relatively coarse grained olivine (300–500 μm) with rounded to flattened orthopyroxene porphyroclasts (~ 5 mm) (Fig. 3.2a). Exsolution of clinopyroxene was common in the core of the orthopyroxene porphyroclasts (Fig. 3.2a). The maximum aspect ratio (X:Z ratio) of flattened

orthopyroxene porphyroclasts approached 5:1, and they generally showed undulose extinctions and kink bands. Olivine crystals were usually elongated parallel to the lineation, and the olivine-olivine grain boundary was normally straight. In olivine dominated areas, relatively large olivine porphyroclasts were common, with small amounts of recrystallized and polygonal olivines (Fig. 3.2e). Sub-grain boundaries and 120° triple junctions were well-developed in olivines (Fig. 3.2e), and sub-grains were more often observed in large grains than small ones.

Proto-mylonitic to mylonitic peridotite (harzburgite; YG-7) exhibited two different texture domains, with areas of relatively coarser (proto-mylonite) and finer (mylonite) olivines (Fig. 3.2b). The grain size and texture of the relatively coarser olivine domain (Fig. 3.2f) was similar to that from the proto-mylonite peridotite (Fig. 3.2e), but the relatively finer olivine domain had polygonal shaped grains, 160–180 μm in size (Fig. 3.2g). Both domains exhibited stretched orthopyroxene and spinel porphyroclasts, and sub-grain boundaries with 120° triple junctions in olivine (Fig. 3.2f and g).

Mylonitic peridotite (harzburgite; YG-8) was characterized by relatively small olivine grains (150–170 μm), with stretched orthopyroxene porphyroclasts (Fig. 3.2c) with maximum aspect ratio approaching 10:1. The clinopyroxene and amphibole content of the matrix was a little higher in the mylonite than in the proto-mylonite (Table 3.1). Although 120° triple junctions were commonly observed in the polygonal shaped olivine dominated matrix, sub-grain boundaries were not common (Fig. 3.2g).

Ultra-mylonitic peridotites (lherzolites; YG-9, 10) were characterized by very fine olivine grains (14–20 μm) with highly stretched orthopyroxene (10–20 mm) and spinel porphyroclasts (Fig. 3.2d). Minor olivine and clinopyroxene porphyroclasts were more commonly observed in ultra-mylonitic peridotite (Fig. 3.2d). The maximum aspect ratios of stretched orthopyroxene porphyroclasts approached 50:1. Undulose extinctions and kink bands were commonly observed in orthopyroxene porphyroclasts. Recrystallized narrow zones were well-developed around orthopyroxene porphyroclasts (Fig. 3.2d and 3.3a), and were composed of relatively polygonal shaped orthopyroxene, olivine, clinopyroxene, and amphibole (pargasite) (Fig. 3.3b). Amphibole neoblasts in the recrystallized narrow zone around orthopyroxene were only present in the ultra-mylonitic peridotite. In the olivine dominated matrix, olivine crystals exhibited well-developed SPO and elongated shapes with undulose extinction and closely spaced sub-grains (Fig. 3.2h), but some of the finer olivine crystals had polygonal shapes with 120° triple junctions. The ultra-mylonitic peridotites had the highest matrix clinopyroxene and amphibole content (Table 3.1), and the only occurrence of fluid inclusion trails, which were common in olivine porphyroclasts (Fig. 3.2i).

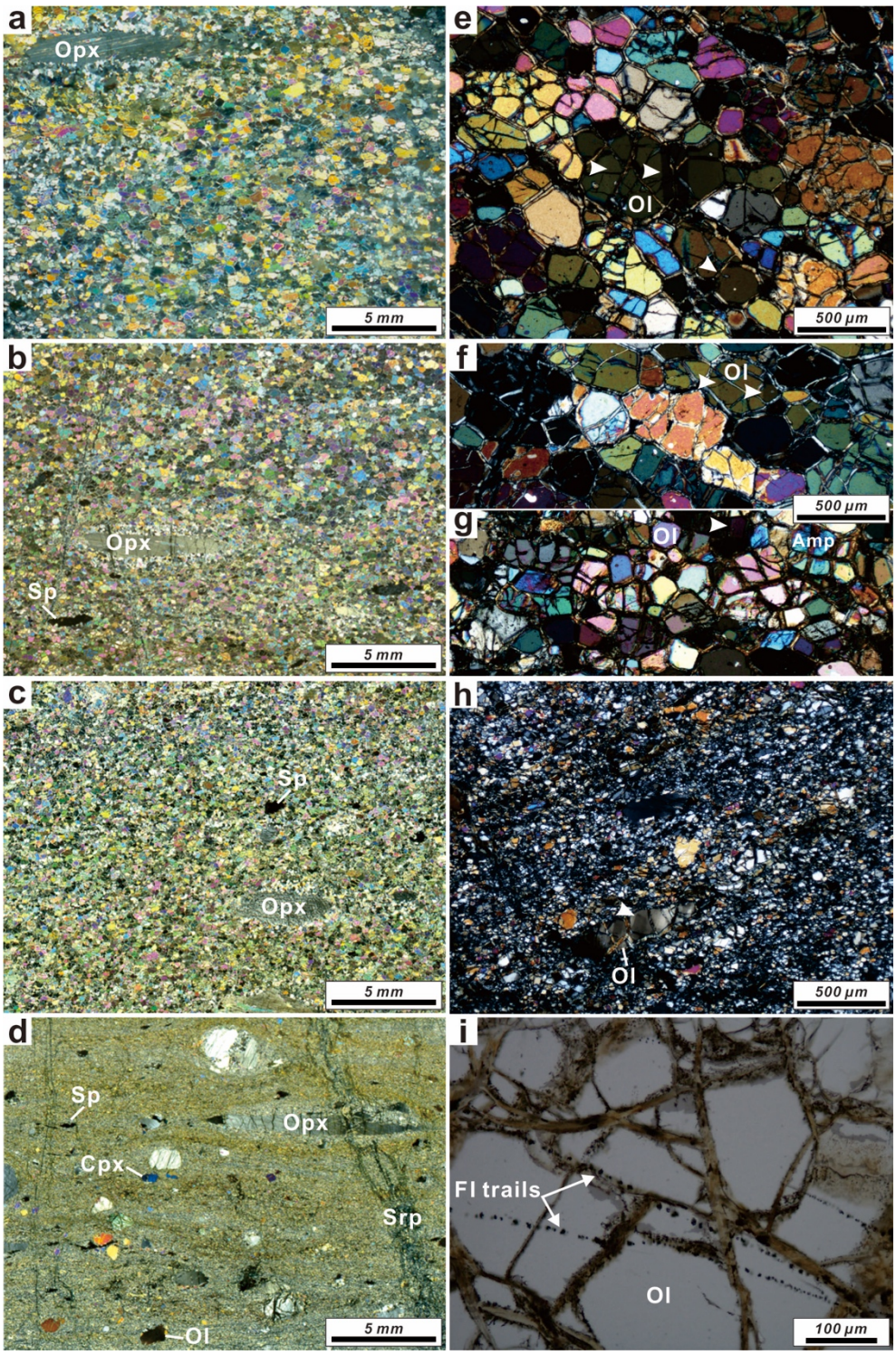

Fig. 3.2. Optical photomicrographs of large-scale and small-scale thin sections (XZ planes) showing deformation microstructures of samples. The

long axes of the photomicrographs are parallel to the lineation (X) and the short axes are normal to the foliation (Z). (a) Proto-mylonitic peridotite (YG-4). (b) Well-preserved transitional texture from proto-mylonitic (upper part) to mylonitic (lower part) peridotite (YG-7). (c) Mylonitic peridotite (YG-8). (d) Ultra-mylonitic peridotite (YG-10). (e-h) Magnified view of representative microstructures from olivine dominated domains: (e, f) proto-mylonite; (g) mylonite; and (h) ultra-mylonite. (i) Fluid inclusion trails in an olivine porphyroclast in ultra-mylonite (YG-10). Opx (orthopyroxene), Sp (spinel), Ol (olivine), Cpx (clinopyroxene), Amp (amphibole), and FI (fluid inclusion). White arrow heads (e-h) represent sub-grain boundaries.

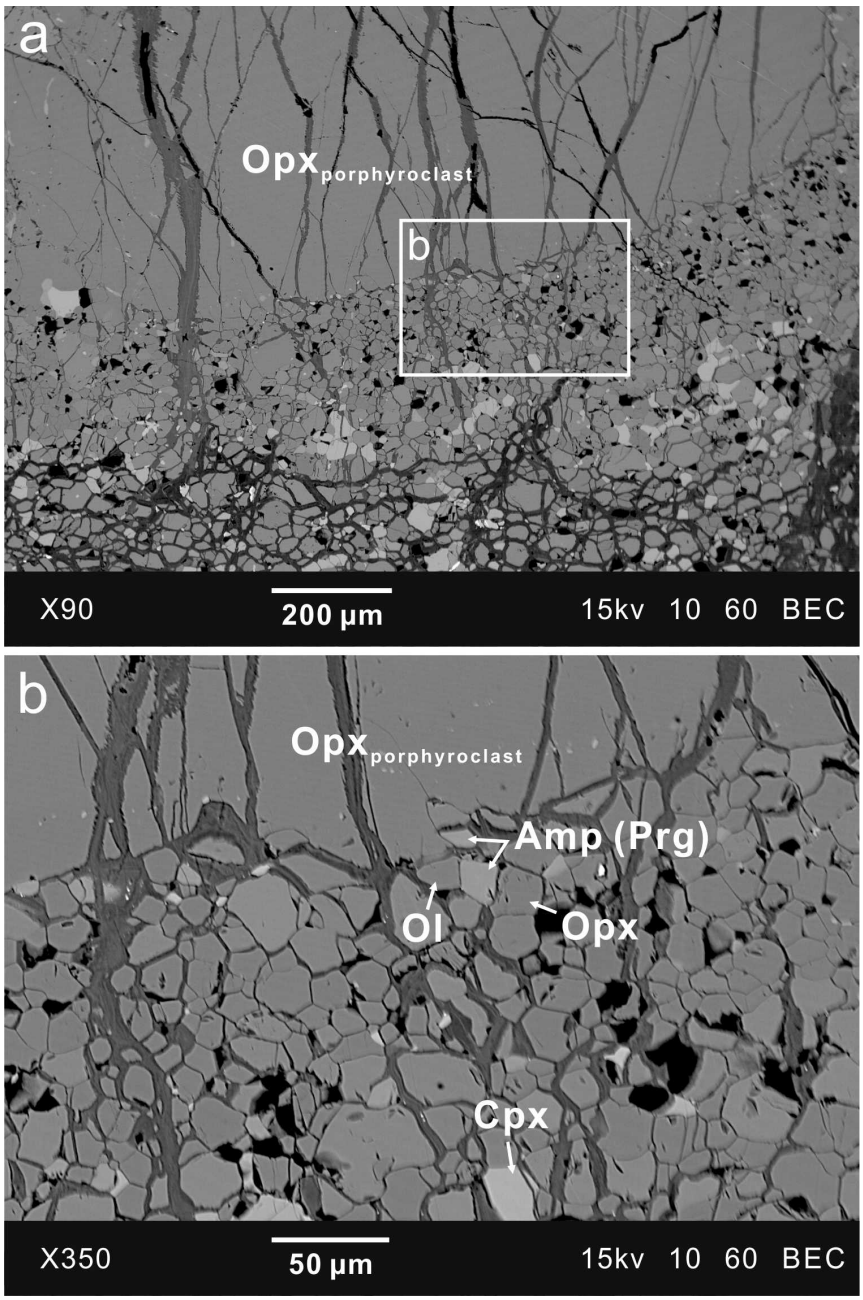

Fig. 3.3. Back-scattered electron images of the narrow recrystallized zone around porphyroclastic orthopyroxene from ultra-mylonitic peridotite (YG-9), consisting of orthopyroxene, olivine, clinopyroxene, and amphibole (pargasite). Opx (orthopyroxene), Ol (olivine), Cpx (clinopyroxene), Amp (amphibole), and Prg (pargasite).

3.5. Dislocation microstructures

XZ-oriented thin-chips were well-polished using 1 μm diamond paste and decorated with oxygen in air at a temperature of 800 °C for 1 h (Karato, 1987), then mounted on glass slides. Dislocation microstructures were observed using both an optical microscope (transmitted light) and a scanning electron microscope (SEM). Back-scattered electron (BSE) images were obtained using a JEOL JSM-7100F field emission SEM at the School of Earth and Environmental Sciences (SEES), Seoul National University (SNU).

Observations revealed numerous dislocations in olivines, shown as reddish dots and lines in the optical photomicrographs (Fig. 3.4a–d) and white dots and lines in the BSE images (Fig. 3.4e and f). In general, the distribution of dislocations was almost inhomogeneous both within and between olivine grains. Straight dislocation walls, indicating sub-grain boundaries, often displayed normal to the lineation (Fig. 3.4a and b). In general, the density of free dislocation olivine porphyroclasts was relatively higher in the ultra-mylonitic peridotites (Fig. 3.4b and f) than the proto-mylonitic and mylonitic peridotites (Fig. 3.4a and e), and the spacing between straight dislocation walls (i.e., sub-grain boundaries) was smaller (Fig. 3.4a and b). In the ultra-mylonitic peridotites, neoblasts showing more polygonal shapes with 120° triple junctions were generally lacking dislocations. However, neoblasts with SPO and elongated shapes (e.g., Fig. 3.2h) still had free dislocations and straight dislocation walls (i.e., sub-grain boundaries) (Fig. 3.4c and d).

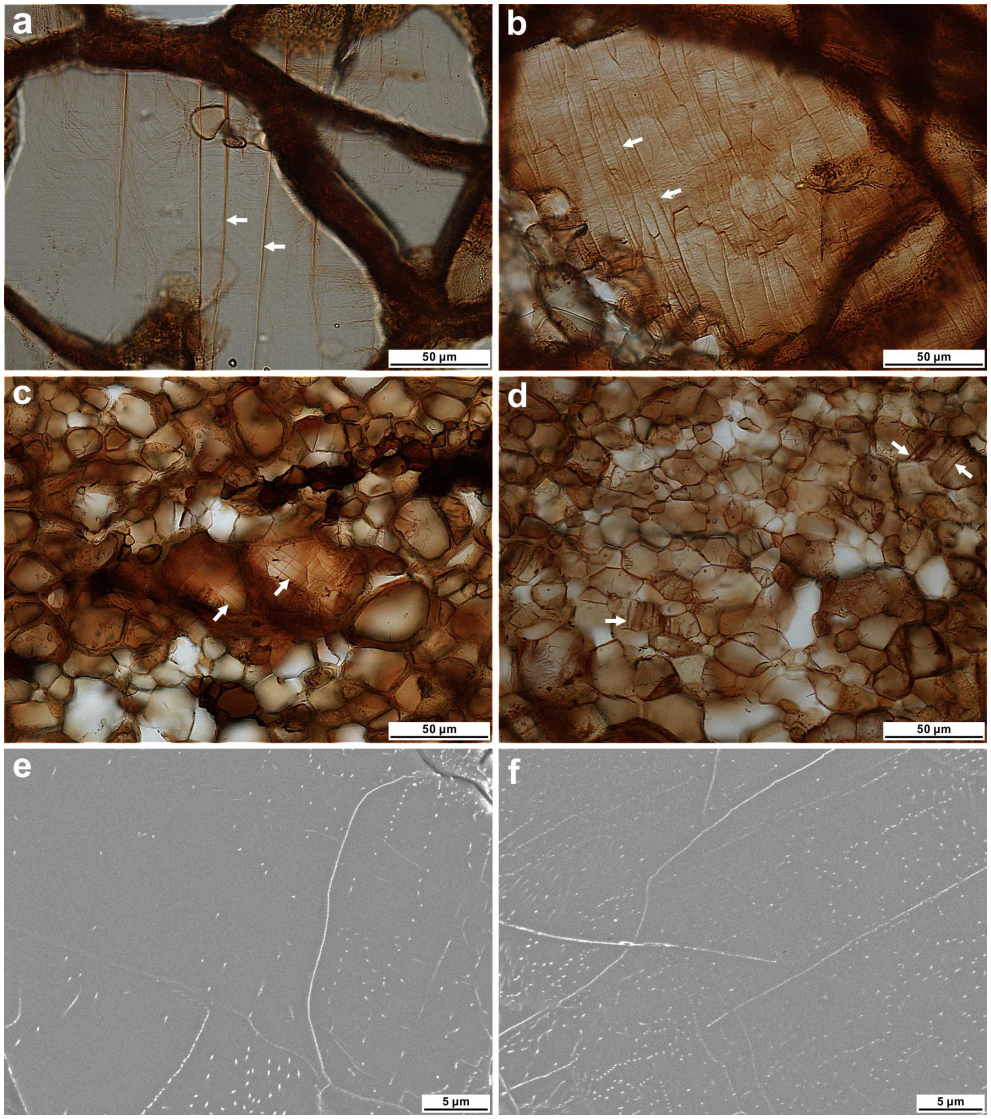

Fig. 3.4. Optical photomicrographs (a-d) and back-scattered electron (BSE) images (e, f) of dislocation microstructures in olivine. Sub-grain boundaries are indicated by white arrows and free dislocations are shown as dots and lines. (a) Dislocation microstructure of olivine porphyroclast in the transitional-textured (proto-mylonite) peridotite (YG-7P) showing low dislocation density. (b) Dislocation microstructure of olivine porphyroclast in

ultra-mylonitic peridotite (YG-10) showing closely spaced sub-grain boundaries and high dislocation density. (c, d) Dislocation microstructure of olivine neoblasts in ultra-mylonitic peridotites (YG-9 and YG-10) showing dislocation-free polygonal and dislocation-bearing elongated grains. (e, f) BSE images of dislocations in olivine porphyroclasts from (e) mylonitic (YG-8) and (f) ultra-mylonitic (YG-9) peridotites.

3.6. Lattice preferred orientation (LPO) and fabric strength of olivine

The LPO of olivine was measured using the electron-backscattered diffraction (EBSD) system hosted at SEES, SNU. The EBSD analysis was conducted in a high vacuum environment with acceleration voltage of 20 kV, working distance of 15 mm, and spot size of 60. We acquired diffraction patterns of olivine in XZ thin section and manually indexed them for accurate solution using HKL CHANNEL 5.0 software. The M-index (Skemer *et al.*, 2005) and J-index (Bunge, 1982) were used to determine olivine fabric (LPO) strength. The M-index delineates differences in uncorrelated misorientation angle distributions between the observed fabric and a theoretical random fabric, and ranges between zero (random fabric) and one (single crystal). The J-index is the volume-averaged integral of the squared orientation density, and ranges from one (random fabric) to infinity (single crystal). The M-index and J-index were calculated using the MTEX toolbox for MATLAB with a kernel half width of 10° (Bachmann *et al.*, 2010).

The results showed a systematic relationship between olivine LPO pattern and rock texture. The LPO of olivine from proto-mylonitic peridotite (YG-4) showed alignment of the [100] axis sub-parallel to the lineation, and the [010] axis was strongly aligned subnormal to the foliation (Fig. 3.5a), which is known as A-type olivine fabric (Jung & Karato, 2001a), representing the dominant slip system of (010)[100]. The LPO of olivine from a

transitional peridotite (proto-mylonite to mylonite; YG-7) represented two different olivine fabrics. The LPO of olivine from the area with proto-mylonitic texture showed A-type olivine fabric (YG-7P) (Fig. 3.5b), while the area with mylonitic texture was characterized by a strong alignment of [100] sub-parallel to the lineation and a weak girdle pattern of [010] and [001] subnormal to the lineation (YG-7M) (Fig. 3.5c), which is known as D-type olivine fabric. This LPO of olivine represents the activation of multiple slip systems of {0kl}[100]. The LPO of olivine from the other sample with mylonitic texture (YG-8) (Fig. 3.5d) was similar to the petrofabric of sample YG-7M (Fig. 3.5c). However, the LPOs of olivine from the ultra-mylonites (YG-9 and YG-10) were different and characterized by an alignment of [100] axes sub-parallel to the lineation and [001] axes subnormal to the foliation (Fig. 3.5e and f), which is known as E-type olivine fabric. They represent the dominant slip system of (001)[100].

The LPO of olivine changed from A-type (proto-mylonites) (Fig. 3.5a and b) via D-type (mylonites) (Fig. 3.5c and d) to E-type (ultra-mylonites) (Fig. 3.5e and f), depending on microstructures of the peridotites. The strength of olivine fabric (M-index and J-index) systematically decreased with decreasing olivine grain size from proto-mylonites via mylonites to ultra-mylonites (Fig. 3.5 and Table 3.1).

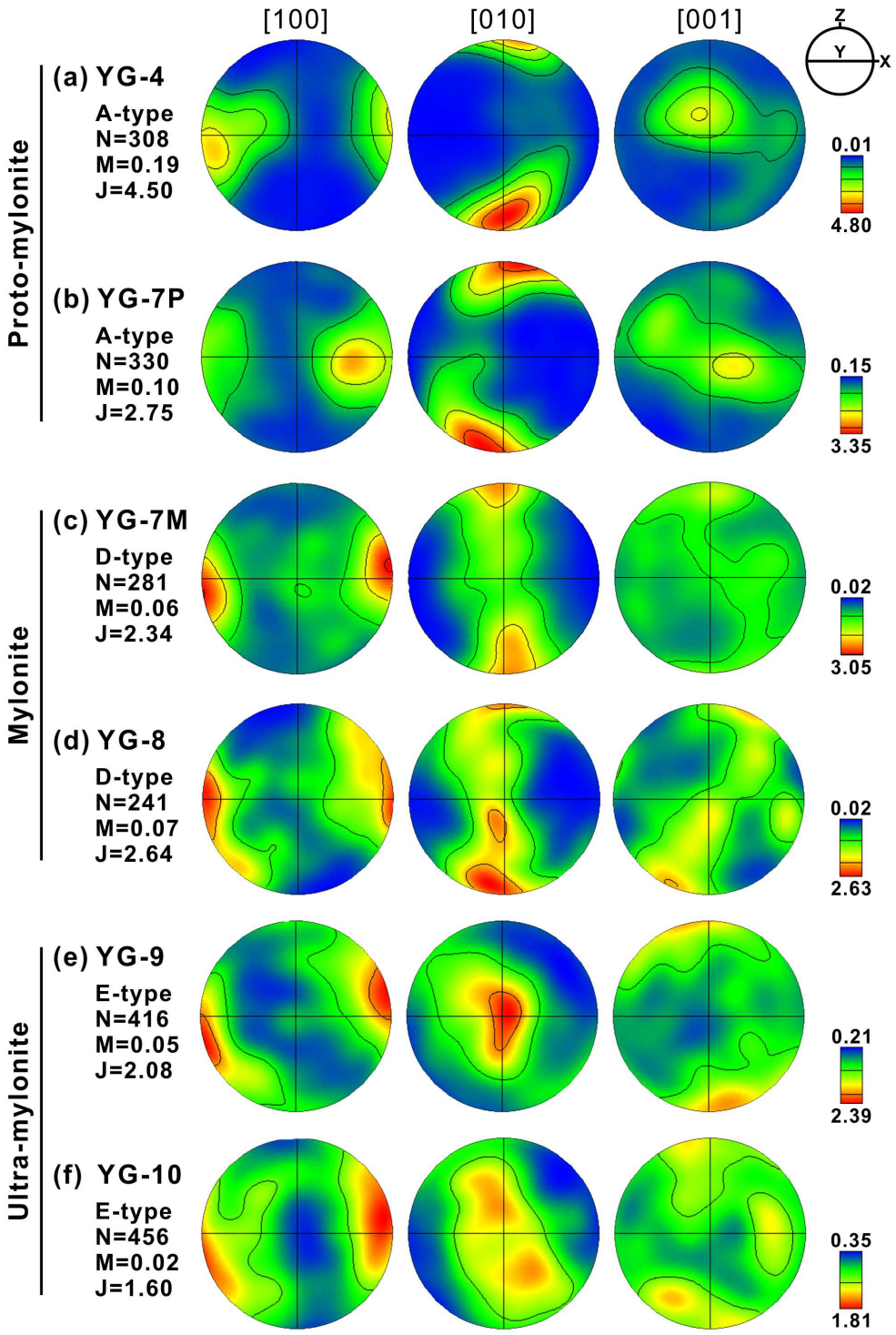

Fig. 3.5. Pole figures showing the lattice preferred orientation (LPO) of olivine. The east-west direction corresponds to stretching lineation (X), and

the north-south direction (Z) is normal to foliation. Color-coding represents the density of data points. Equal-area and lower-hemisphere projection was used with a half scattering width of 30°. N represents the number of measured grains. Olivine fabric (LPO) strength is denoted as M (M-index) (Skemer *et al.*, 2005) and J (J-index) (Bunge, 1982).

3.7. Olivine grain size and paleopiezometry

Olivine grain size was determined by the following method (e.g., Cao et al., 2015): (1) the outline of 200 olivine grains from olivine dominated areas was traced on photomicrographs and back-scattered electron images; (2) the diameter of circles of equivalent areas to measured grains was calculated, and weighted by the number of grains; (3) the number-weighted grain size was multiplied by a factor of 1.12 to convert it to grain size estimated by the linear-intercept method, based on the relationship established by Berger et al. (2011); (4) the 2D grain size was multiplied by a factor of 1.5 to convert it to 3D size. This was used to estimate stress based on the recrystallized grain size piezometers of Karato *et al.* (1980), Van der Wal *et al.* (1993), and Jung and Karato (2001b).

Mean 3D grain-sizes of olivine specimens were as follows: 621−530 μm (proto-mylonites); 322−281 μm (mylonites); and 30−24 μm (ultra-mylonites) (Table 3.1). Calculated stress based on dry paleopiezometers, Karato *et al.* (1980) and Van der Wal *et al.* (1993), was in the range of 9−10 MPa and 11−12 MPa (proto-mylonites), 15−17 MPa and 18−20 MPa (mylonites), 116−141 MPa and 108−127 MPa (ultra-mylonites), respectively. However, the stress calculated for ultra-mylonites using the wet paleopiezometer of olivine (Jung & Karato, 2001b) was higher (280−310 MPa).

3.8. Fourier transform infrared (FTIR) spectroscopy

The structural position of hydroxyl (OH) in nominally anhydrous minerals (olivine and pyroxene) was determined by FTIR spectroscopy using a Nicolet 6700 spectrometer with a Continuum IR Microscope at the Tectonophysics Laboratory, SNU. Prior to IR measurements, doubly polished thin-slices (150−250 μm thick) were placed in an acetone bath for 24 h to remove any residual glue, and then heated to 120 °C for at least 24 h to dispel any free water residing on the surface of the slice and in grain boundaries/cracks. FTIR measurements were performed using an unpolarized light source, a KBr beam splitter, and a mercury cadmium telluride detector cooled with liquid nitrogen, and dry and pure nitrogen gas was flushed into the system to avoid disturbance caused by moisture in the atmosphere. IR spectra were accumulated from an average of 128 scans with a resolution of 4 cm^{-1}.

The structural position of OH in olivines and orthopyroxenes was characterized using unpolarized FTIR spectroscopy (Fig. 3.6). The ultra-mylonitic peridotites showed three IR peaks (3688, 3571, and 3562 cm^{-1}; Fig. 3.6c) relating to hydrous minerals found in olivine, whereas there was no IR peak in both the proto-mylonitic and mylonitic peridotites (Fig. 3.6a). The IR peak at 3688 cm^{-1} is associated with serpentine inclusions (Kitamura *et al.*, 1987; Khisina *et al.*, 2001; Matsyuk & Langer, 2004; Jung, 2009), and the peaks at 3571 and 3562 cm^{-1} are possibly related to Ti-clinohumite defects

(Kitamura *et al.*, 1987; Berry *et al.*, 2005; Hermann *et al.*, 2007; De Hoog *et al.*, 2014). Small IR peaks of serpentine (3688 cm^{-1}; Fig. 3.6b) were rarely observed in orthopyroxenes from the proto-mylonitic and mylonitic peridotites. In contrast, stronger serpentine peaks were often observed in orthopyroxene from the ultra-mylonitic peridotites (Fig. 3.6d).

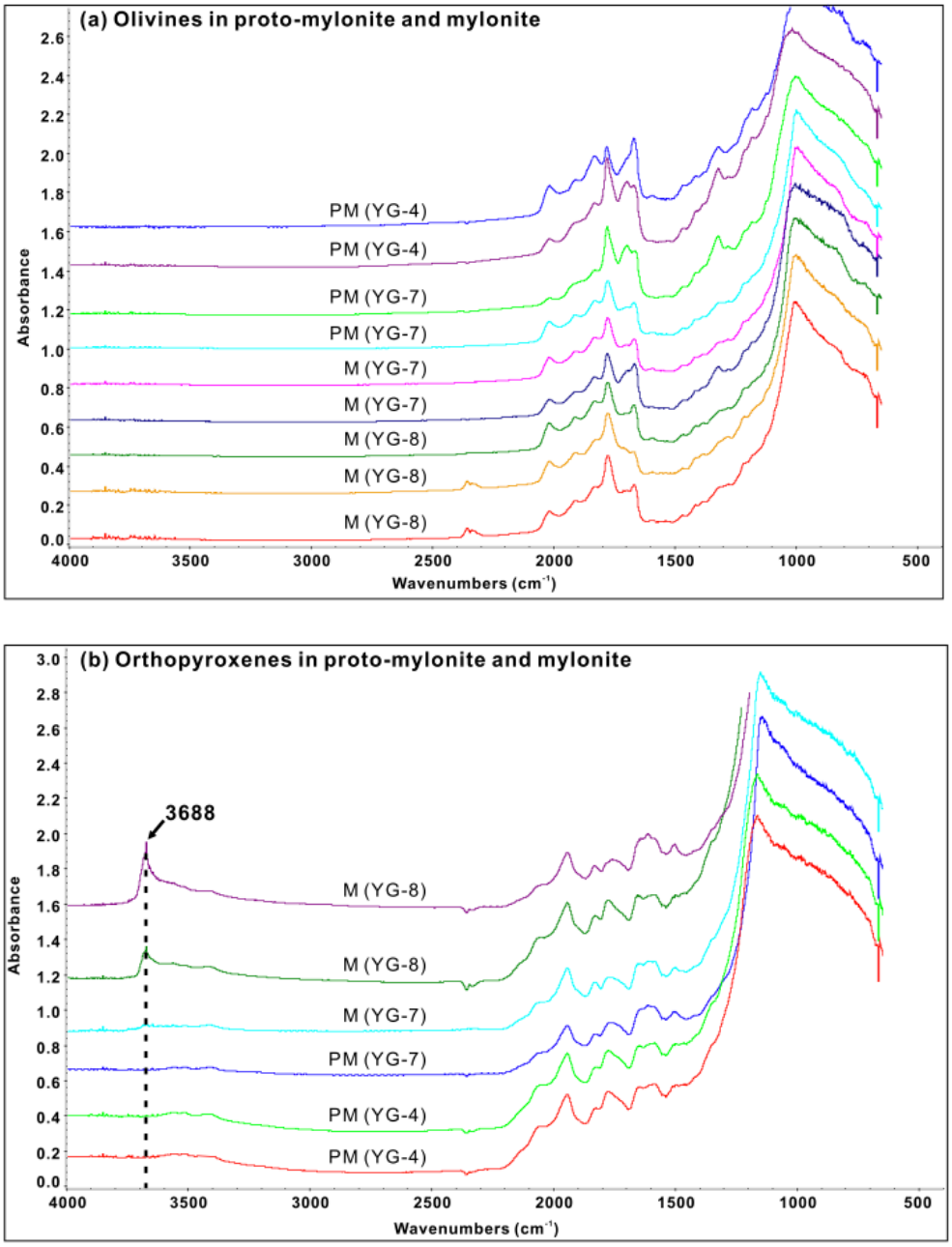

Fig. 3.6. Unpolarized IR spectra for representative olivine and orthopyroxene from proto-mylonitic (PM) and mylonitic (M) peridotites (a, b) and ultra-mylonitic (UM) peridotites (c, d).

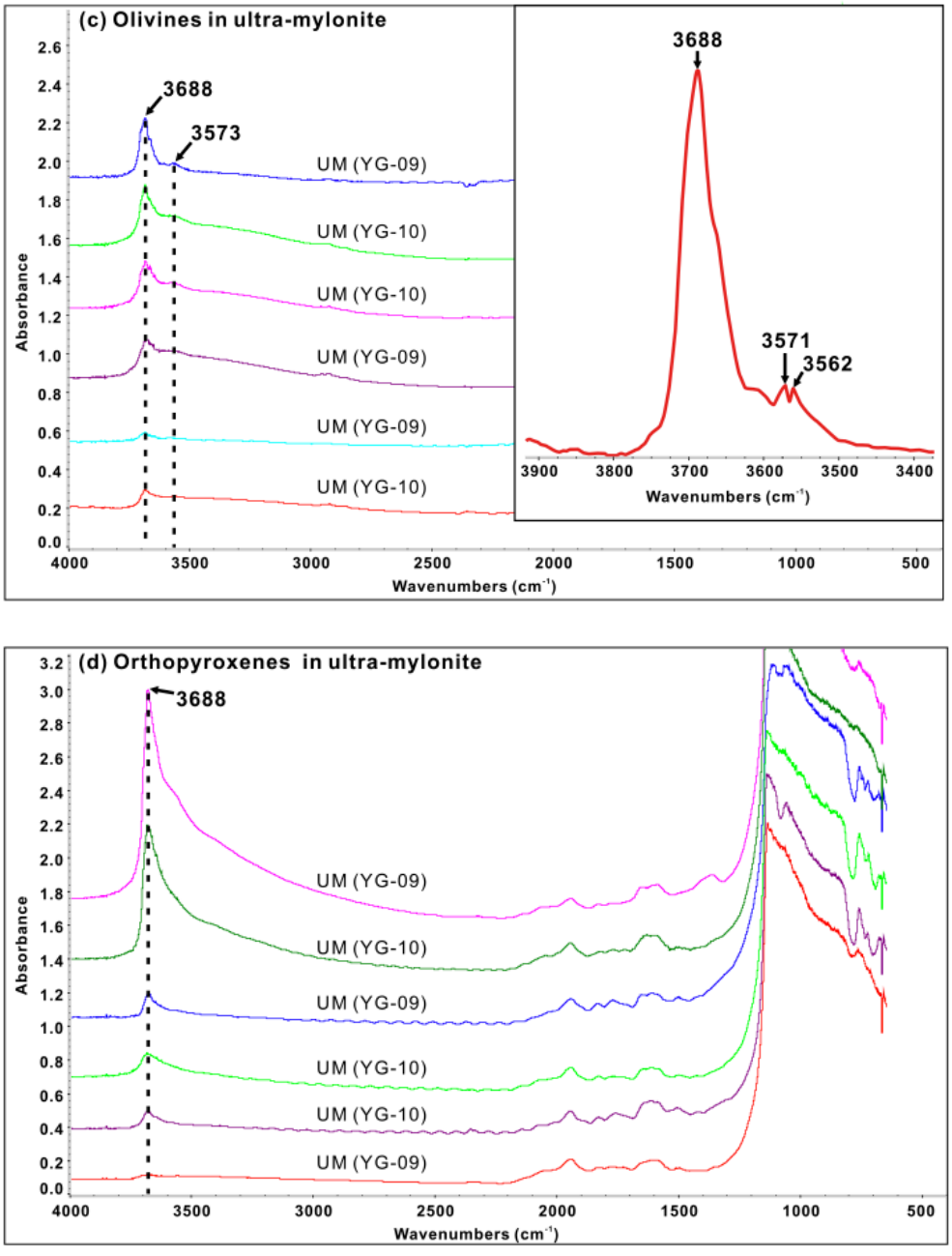

Fig. 3.6. (continued)

3.9. Mineral chemistry

The chemical composition of minerals was determined by electron microprobe analysis using a JEOL JXA-8100 wavelength-dispersive electron microprobe with ZAF matrix correction at the Gyeongsang National University in Jinju, South Korea. Operating conditions comprised 15 kV accelerating voltage, 10 nA beam current, 5 μm beam width, and 20 s counting time. Natural minerals were used as standards for Si, Ti, Al, Fe, Mn, Mg, Ca, Na, and K, with synthetic oxides for Cr and Ni. Representative microprobe analysis results are given in Table 3.2.

The electron microprobe analysis was performed on the cores of neoblasts in the olivine dominated area due to a lack of olivine porphyroclasts. The olivine Mg-number was 0.90−0.91 in harzburgites and 0.89 in lherzolites, and decreased from proto-mylonites (0.91) via mylonites (0.90) to ultra-mylonites (0.89). NiO content was in the range of 0.31−0.56 wt% for all peridotites, and there was no correlation between NiO content and lithology.

For spinel, there was a clear distinction in Al_2O_3 and Cr_2O_3 content between harzburgites and lherzolites. Spinel Cr-numbers, 0.216−0.293 in harzburgites and 0.118−0.130 in lherzolites, generally displayed a positive correlation with olivine Mg-numbers. The relationship between the olivine Mg-number (or Fo content) and spinel Cr-number in the olivine-spinel mantle array (e.g., Arai *et al*., 2008) indicates that the petrogenetic setting of our specimen is abyssal peridotite.

Table 3.2. Representative electron microprobe analyses of minerals in the Yugu peridotites.

Sample	YG4_Hzb (Proto-mylonite)					YG7_Hzb (Proto-mylonite to mylonite)					YG8_Hzb (Mylonite)				
Mineral	Ol	Opx			Sp	Ol	Opx			Sp	Ol	Opx			Sp
		core	rim	neoblast			core	rim	neoblast			core	rim	neoblast	
SiO_2	40.50	56.00	57.06	57.33	0.00	40.63	56.03	57.25	57.41	0.01	40.69	56.00	57.16	57.20	0.00
TiO_2	0.00	0.07	0.00	0.00	0.04	0.00	0.04	0.00	0.00	0.03	0.00	0.07	0.02	0.01	0.02
Al_2O_3	0.00	3.16	1.54	1.20	48.39	0.00	3.22	1.58	1.06	45.10	0.00	3.11	1.33	1.06	42.09
Cr_2O_3	0.00	0.41	0.12	0.12	19.88	0.00	0.43	0.15	0.08	22.81	0.01	0.41	0.05	0.06	26.06
FeO	9.20	6.60	6.45	6.35	15.15	9.24	6.37	6.48	6.46	16.71	9.75	6.60	6.42	6.29	17.27
MnO	0.14	0.18	0.16	0.18	0.17	0.18	0.20	0.13	0.14	0.22	0.12	0.17	0.17	0.17	0.25
MgO	49.51	32.98	33.71	33.73	15.76	49.52	32.90	33.61	34.29	15.12	48.51	32.98	33.83	34.08	14.26
CaO	0.01	0.27	0.18	0.20	0.03	0.00	0.29	0.20	0.24	0.00	0.03	0.22	0.15	0.21	0.01
Na_2O	0.00	0.00	0.01	0.00	0.00	0.00	0.01	0.00	0.01	0.02	0.00	0.00	0.00	0.00	0.01
K_2O	0.00	0.01	0.00	0.00	0.00	0.00	0.01	0.01	0.00	0.00	0.00	0.01	0.01	0.02	0.00
NiO	0.45	0.09	0.08	0.07	0.14	0.56	0.01	0.08	0.05	0.17	0.32	0.09	0.05	0.05	0.10
Totals	99.81	99.77	99.31	99.18	99.55	100.13	99.51	99.49	99.74	100.19	99.43	99.66	99.19	99.15	100.07
$Mg^{\#}$	0.906	0.899	0.903	0.905	0.650	0.906	0.902	0.902	0.904	0.617	0.899	0.899	0.904	0.906	0.595
$Cr^{\#}$					0.216					0.253					0.293

$Mg^{\#}$ = Mg/(Mg +Fe); $Cr^{\#}$ = Cr/(Cr + Al).

Table 3.2. (continued)

Sample	YG9_Lhz (Ultra-mylonite)								YG10_Lhz (Ultra-mylonite)							
Mineral	Ol	Opx			Sp	Cpx		Amp	Ol	Opx			Sp	Cpx		Amp
		core	rim	neoblast		core	rim			core	rim	neoblast		core	rim	
SiO_2	40.87	54.61	55.96	56.73	0.00	50.87	51.57	43.42	40.83	54.75	55.68	56.79	0.00	51.38	52.46	43.34
TiO_2	0.06	0.08	0.07	0.01	0.01	0.31	0.30	0.98	0.00	0.03	0.02	0.05	0.07	0.32	0.31	1.45
Al_2O_3	0.01	4.45	2.93	1.77	56.57	6.16	5.15	14.73	0.01	4.60	2.96	1.60	55.55	5.68	4.81	14.26
Cr_2O_3	0.00	0.42	0.29	0.14	11.32	0.87	0.76	0.83	0.04	0.43	0.26	0.15	12.35	0.72	0.66	0.55
FeO	10.54	6.95	6.72	6.86	12.41	2.79	2.59	4.08	10.65	7.31	7.14	7.08	12.73	2.46	2.53	4.06
MnO	0.19	0.15	0.21	0.16	0.12	0.09	0.11	0.05	0.15	0.17	0.17	0.13	0.15	0.10	0.07	0.05
MgO	47.87	32.03	32.58	33.16	19.12	14.36	14.78	16.74	47.90	32.21	32.52	33.31	18.67	14.76	14.83	16.72
CaO	0.00	0.31	0.21	0.30	0.00	22.35	23.00	12.58	0.04	0.29	0.25	0.27	0.01	22.76	23.30	12.74
Na_2O	0.00	0.00	0.00	0.00	0.00	1.13	0.86	2.70	0.00	0.02	0.00	0.01	0.00	0.93	0.85	2.63
K_2O	0.01	0.00	0.00	0.00	0.00	0.02	0.00	0.10	0.01	0.02	0.01	0.01	0.00	0.00	0.00	0.15
NiO	0.34	0.02	0.04	0.08	0.30	0.06	0.01	0.07	0.31	0.04	0.03	0.06	0.36	0.04	0.04	0.07
Totals	99.89	99.02	99.01	99.21	99.85	99.01	99.13	96.28	99.94	99.87	99.04	99.46	99.90	99.16	99.86	96.02
$Mg^{\#}$	0.890	0.891	0.896	0.896	0.733	0.902	0.910	0.880	0.889	0.887	0.890	0.893	0.724	0.914	0.913	0.880
$Cr^{\#}$					0.118								0.130			

$Mg^{\#}$ = Mg/(Mg +Fe); $Cr^{\#}$ = Cr/(Cr + Al).

For orthopyroxene, all the analyzed grains were enstatite-rich with Mg-numbers ranging from 0.89 to 0.91. There was a distinct difference between orthopyroxene porphyroclast cores and rims, and the composition of orthopyroxene neoblasts was similar to the porphyroclastic rims. The Al_2O_3 content of orthopyroxene porphyroclasts decreased toward the rim in harzburgites (3.22 → 1.33 wt%) and lherzolites (4.60 → 2.93 wt%), whereas SiO_2 content increased in harzburgites (56.00 → 57.25 wt%) and lherzolites (54.61 → 55.96 wt%). The Cr_2O_3 content of orthopyroxene porphyroclasts decreased toward the rim (0.43 → 0.05 wt%), while MgO increased (32.03 → 33.83 wt%). Compared with orthopyroxene porphyroclasts cores, orthopyroxene neoblasts displayed lower levels of Al_2O_3 (1.06−1.77 wt%) and Cr_2O_3 (0.06−0.15 wt%), and higher levels of MgO (33.16−34.29 wt%).

For clinopyroxene, Mg-numbers ranged from 0.90 to 0.91, and there were clear compositional trends from core to rim of porphyroclasts in lherzolites. Both Al_2O_3 and Cr_2O_3 decreased (6.16 → 4.81 wt% and 0.87 → 0.66 wt%, respectively) from core to rim, whereas MgO slightly increased (14.36 → 14.83 wt%). CaO and SiO_2 increased toward the rim (22.35 → 23.30 wt% and 50.87 → 52.46 wt%, respectively) while Na_2O decreased (1.13 → 0.85 wt%).

Amphiboles were all pargasites and their Mg-numbers (0.88) were slightly lower than those for coexisting olivine and pyroxenes. The pargasites had low content of Na_2O (<2.70 wt%), TiO_2 (<1.45 wt%), and K_2O (<0.15 wt%).

3.10. Thermometry

Porphyroclast (PC) and neoblast (NB) equilibrium temperatures in this study were calculated based on the following formulations: (1) a thermometer based on coexisting orthopyroxene and clinopyroxene ($T_{Two\text{-}pyx\ Wells77}$) (Wells, 1977) for PC; (2) orthopyroxene Al and Cr content ($T_{Al,Cr\text{-}in\text{-}opx\ WS91}$) (Witt-Eickschen & Seck, 1991) for PC and NB; (3) the Ca-in-opx thermometer ($T_{Ca\text{-}in\text{-}opx\ BK90}$) (Brey & Köhler, 1990) for NB. Pressure was assumed to be 0.5 GPa for the Ca-in-opx thermometer calculations. If we were instead assumed a pressure of 1 GPa, the calculated temperatures would increase by 20 °C. The error ranges of the thermometers $T_{Two\text{-}pyx\ Wells77}$, $T_{Al,Cr\text{-}in\text{-}opx\ WS91}$, and $T_{Ca\text{-}in\text{-}opx\ BK90}$ were ± 70 °C, ± 16 °C, and ± 19 °C, respectively.

For PC, the results of Wells (1977) and Witt-Eickschen and Seck (1991) thermometers give temperatures of 990−1130 °C and 920−1000 °C, respectively. However, for NB, application of the Brey and Köhler (1990) and Witt-Eickschen and Seck (1991) thermometers give 700−760 °C and 710−760 °C, respectively. These results show no clear relationship between proto-mylonite, mylonite, and ultra-mylonite even though there is a temperature difference between porphyroclasts and neoblasts. Moreover, the temperature difference is generally consistent with a previous study which gave ~1000 °C for porphyroclasts and ~800 °C for neoblasts (Arai *et al.*, 2008).

3.11. Discussion

3.11.1 Olivine fabric transition in the mantle shear zone

The results showed that the LPO of olivine varied with textural type for the Yugu peridotites, from A-type (proto-mylonites) (Fig. 3.5a and b) via D-type (mylonites) (Fig. 3.5c and d) to E-type (ultra-mylonites) (Fig. 3.5e and f). Proto-mylonitic peridotites showed A-type olivine fabrics. In general, A-type olivine fabric has been observed at high temperature, low water content, and low stress conditions in previous experimental studies (Zhang & Karato, 1995; Zhang *et al.*, 2000; Jung & Karato, 2001a; Demouchy *et al.*, 2012; Hansen *et al.*, 2012) and in natural samples (Michibayashi & Mainprice, 2004; Jung *et al.*, 2009; Falus *et al.*, 2011; Park *et al.*, 2014). Although the equilibrium temperature estimated from orthopyroxene rim neoblasts in the proto-mylonitic peridotites is low, in the range of 700−760 °C, it does not necessarily mean that the LPO was formed at low temperature. The olivine dominated area of proto-mylonitic peridotites consists of porphyroclastic olivines with few polygonal neoblasts (Fig. 3.2e and f), whereas that of the mylonitic and ultra-mylonitic peridotites consists of predominantly small polygonal neoblasts (Fig. 3.2g and h). Moreover, there was no hydrous mineral IR peak in olivine from the proto-mylonitic peridotites (Fig. 3.6a). Therefore, A-type olivine fabric in the proto-mylonitic peridotites is thought to have been preserved from the original fabric which was formed under high

temperature (~1000 °C), low stress, and dry conditions, before shear localization related deformation. However, the presence of polygonal shaped neoblasts indicate the high temperature A-type fabric was relatively weakened by dynamic recrystallization at a lower temperature (Fig. 3.2e).

In the mylonitic peridotites, olivine LPOs show D-type fabric, which is relatively common in lithospheric shear zones (ophiolites at low temperature and high stress) (e.g., Warren *et al*., 2008; Skemer *et al*., 2010; Linckens *et al*., 2011; Michibayashi & Oohara, 2013; Kaczmarek *et al*., 2015). Possible mechanisms for formation of D-type olivine fabric include: (1) activation of multiple {0kl}[100] slip systems at lower water and higher stress conditions, than A-type olivine fabrics (Bystricky *et al.*, 2000; Zhang *et al.*, 2000; Jung *et al.*, 2006); (2) activation of only the (010)[100] slip system under transtensional deformation regimes (Tommasi *et al.*, 1999); (3) activation of dominant (010)[100] and (001)[100] slip systems at high temperature and low stress conditions, with strain compatibility constraints relaxed by grain-to-grain interactions (Tommasi *et al.*, 2000), or dislocation accommodated grain boundary sliding (Warren *et al.*, 2008; Hansen *et al.*, 2012) under moderate transient strain conditions (Hansen *et al.*, 2014).

As discussed above, olivines from our mylonitic peridotites were mostly recrystallized and had polygonal and equigranular textures, whereas olivines from the proto-mylonitic peridotites were generally characterized by a relatively coarse texture with porphyroclasts (porphyroclastic texture). This change of texture suggests that mylonitic peridotites were affected by

deformation during shear localization at low temperature (700−760 °C) and high stress (moderate strain) conditions relative to proto-mylonites (A-type olivine fabric). Moreover, the Yugu mylonitic peridotites also display olivine fabrics of a transitional character (Fig. 3.5c and d), between high temperature A-type (proto-mylonite) and low temperature E-type (ultra-mylonite). The D-type olivine fabric, found in the mylonitic peridotites in this study, is considered to represent a mixture of (010)[100] and (001)[100] slip systems, resulting from the change in deformation conditions (e.g., Sawaguchi, 2004; Kamei *et al*., 2010).

In ultra-mylonitic peridotites, olivine LPOs represent the E-type fabric. This type of fabric is considered to be widespread in the asthenosphere (Karato *et al.*, 2008). The E-type fabrics were reported in collision zones (Sawaguchi, 2004; Jung, 2009; Jung *et al.*, 2014), island oceanic arc environments (Mehl *et al.*, 2003), extensional settings such as shear zones within oceanic lithosphere (Michibayashi & Mainprice, 2004; Skemer *et al.*, 2010; Linckens *et al.*, 2011; Michibayashi & Oohara, 2013), and rifting environments (Palasse *et al.*, 2012; Kaczmarek & Reddy, 2013). The formation context of E-type olivine fabric has been suggested by previous studies as wet conditions (Katayama *et al.*, 2004; Jung *et al.*, 2006; Jung, 2009; Skemer *et al.*, 2010; Michibayashi & Oohara, 2013), low temperatures (Carter & Ave'Lallement, 1970; Kamei *et al.*, 2010; Linckens *et al.*, 2011), and at a high temperature with high melt content (Tommasi *et al.*, 2006).

In the Yugu peridotites, estimated neoblast temperatures are similar

for mylonite and ultra-mylonite, at 700−760 °C, which means that the different olivine fabrics in the study area were not related to high temperature conditions (with/without melt). Previous extensive experiments on the formation of E-type LPO in olivine (Katayama *et al.*, 2004; Jung *et al.*, 2006) have shown that the dominant (001)[100] slip system can be formed under moderate water content (wet conditions). Moreover, most previous studies of E-type olivine fabrics in natural mantle shear zones (Sawaguchi, 2004; Skemer *et al.*, 2010; Michibayashi & Oohara, 2013; Jung *et al.*, 2014) have reported formation of the slip system under wet conditions. In our ultra-mylonitic peridotites with E-type olivine fabrics, we also found indicators of H_2O activity such as Ti-clinohumite defects (and serpentine) (Fig. 3.6c) and fluid inclusion trails (Fig. 3.2i) in elongated olivine porphyroclasts, and a hydrous mineral (pargasite) in the matrix (Table 3.1 and Fig. 3.3b). Hydrous fluid/melt was probably supplied from the dehydration of the surrounding crustal rock due to shear localization (Sawaguchi, 2004), as our ultra-mylonitic peridotites are located in marginal areas of peridotites, adjacent to migmatitic gneisses (basement rock). This scenario is also supported by a previous geochemical study by Arai *et al.* (2008) on U-shaped rare earth element (REE) patterns in clinopyroxenes and amphiboles from Yugu lherzolites. They concluded that hydration was associated with enrichment in light REE, resulting from either a fluid circulating in the crust or a slab-derived fluid. Recently, Tasaka *et al.* (2016) conducted torsion experiments of olivine aggregates under hydrous conditions (T=1200 °C and P=300 MPa)

and observed (001)[100] and (100)[001] slip at high strain ($\gamma \geq 3.4$). However, Hansen *et al.* (2014) carried out similar torsion experiments under anhydrous conditions and found that the [100] axes form a strong point maxima and both the [010] and [001] axes are strongly distributed as a girdle (D-type) at similar shear strain (γ: 3−5), with a fabric transition to A-type fabric at high shear strains. These observations indicate that activation of the olivine (001)[100] slip system representing E-type fabric cannot be explained without the presence of water. Therefore, E-type olivine fabrics in the Yugu ultramylonitic peridotites are interpreted as forming under hydrous conditions at low temperature and high strain. It is worth noting that water is a significant factor for enhancing shear strain, and can produce a transition from pre-existing fabric in the mantle shear zone.

One further interesting point is that our E-type fabric is unique in terms of its relatively small olivine grain size (24−30 μm in 3D) for a mantle shear zone context. Most E-type fabrics previously described from natural mantle shear zones have coarser olivine grains, such as 257−646 μm (Michibayashi & Oohara, 2013), ~250 μm (Skemer *et al.*, 2010), and 110−350 μm (Linckens *et al.*, 2015). E-type olivine fabric with very small grains, 10−20 μm in size, has been previously reported only from mylonitic and ultramylonitic xenoliths in the East African Rift (Kaczmarek & Reddy, 2013).

3.11.2 Mechanism of olivine deformation in the mantle shear zone

The three main olivine deformation mechanisms are dislocation

creep, diffusion creep, and dislocation accommodated grain boundary sliding (DisGBS). All three mechanisms can operate at the same time, but with one mechanism dominant. Based on microstructural observations of naturally and experimentally deformed specimens, the transitions from dislocation creep to DisGBS, and between dislocation creep and diffusion creep (Hirth & Kohlstedt, 1995), have been considered as major sources of strain localization in the Earth's lithosphere (Warren & Hirth, 2006; Hansen *et al.*, 2011; 2012). Based on microstructural analyses of mylonite fabric in naturally deformed peridotites, Warren and Hirth (2006) suggested that an LPO is maintained during DisGBS when the easy slip component is dominant during deformation (grain size 10–100 μm), though rate limited by the GBS component. In addition, deformation experiments of olivine aggregates (Hansen *et al.*, 2012) showed dislocations, sub-grain structures with SPO (grain size 7–27 μm), and the development of a strong LPO in the DisGBS regime.

Proto-mylonitic peridotites in the Yugu peridotite body showed strong olivine LPOs (Fig. 3.5a and b) which were interpreted as the result of deformation at high temperature (A-type olivine fabric). Those strong LPOs and numerous dislocations in olivine (Fig. 3.4a) indicate that proto-mylonitic peridotites were deformed by dislocation creep. Mylonitic peridotites had weaker olivine LPOs (D-type olivine fabric) than the proto-mylonitic peridotites and fabric strength (M- and J-index) sharply decreased (Fig. 3.5c and d), with grain size reduction, while polygonal shaped olivines increased

in number (Fig. 3.2g). However, some olivines still contained dislocations (Fig. 3.4e). These microstructure characteristics indicate a transition in the deformation mechanism from dislocation creep to DisGBS. Finally, in the ultra-mylonitic peridotites, E-type olivine LPOs were developed with extreme grain size reduction (24−30 μm) and fabric strength was lower (Fig. 3.5e and f) than that of the mylonitic peridotites. Neoblast dislocation microstructures in the ultra-mylonitic peridotites showed two characteristics: (1) elongated grains with straight dislocation walls; and (2) polygonal grains lacking dislocations. Therefore, we infer that the ultra-mylonitic peridotites were deformed by DisGBS with a dominant (001)[100] olivine slip system.

3.12. Conclusions

We reported on well-preserved transitional characteristics of olivine microstructures and LPOs found in the mantle shear zone of the Yugu peridotite body in the Gyeonggi Massif, Korea. The Yugu peridotite body predominantly comprises spinel harzburgite together with minor lherzolite, dunite, and clinopyroxenite. We classified highly deformed peridotites into four textural types, based on their microstructural characteristics (especially olivine grain size): proto-mylonite; proto-mylonite to mylonite transition; mylonite; and ultra-mylonite. The proportion of clinopyroxene and amphibole increased toward ultra-mylonitic peridotites. Olivine LPO varied with textural type of specimens, from A-type (proto-mylonites) via D-type

(mylonites) to E-type (ultra-mylonites). The olivine fabric transition from A-type to E-type is interpreted to have occurred under hydrous conditions at low temperature (700−760 °C) and high strain, based on characteristics such as Ti-clinohumite defects (and serpentine) and fluid inclusion trails in olivine, and a hydrous mineral (pargasite) in the matrix, especially from the ultra-mylonitic peridotites. Olivine fabric strength (M- and J-index) systematically decreased with decreasing olivine grain size from proto-mylonite via mylonite to ultra-mylonite. Even though the grain size of neoblasts in the ultra-mylonitic peridotites was extremely small (24−30 μm), olivine fabrics showed a clear E-type pattern rather than random fabric. Analysis of the LPO strength, dislocation microstructures, and olivine grain size suggest that the proto-mylonitic peridotites were deformed by dislocation creep, whereas both the mylonitic and ultra-mylonitic peridotites were deformed by DisGBS.

CHAPTER 4

Conclusions

This thesis presents detailed analysis of fluid inclusions (Chapter 2) and deformation microstructures (Chapter 3) from naturally deformed peridotites in order to understanding the origin and evolution history of upper mantle rocks related to geodynamics.

In Chapter 2, fluid inclusions trapped in orthopyroxene porphyroclasts in spinel peridotite xenoliths from Adam's Diggings (AD), the rift shoulder of the Rio Grande Rift (RGR), were the subject. Results from fluid inclusion petrography together with various analytical results (microthermometry, Raman spectroscopy, and Focused Ion Beam-Scanning Electron Microscopy) indicated that there were at least two fluid invasions beneath the RGR mantle with different fluid compositions and at different times. The Type-1 FIs (C–O–N–S) in orthopyroxenes were trapped from the earlier fluid invasion during a cooling event. In the meantime, clinopyroxene and spinel lamellae exsolved from the high-temperature orthopyroxene. The Type-2 FIs (C–O–H–S) entrapped following the formation of the orthopyroxene represent a later stage fluid invasion. The two fluid invasions in the AD peridotites indicated the complexity of mantle fluids in the RGR. However, further isotopic and chemical studies are needed to understand the relationship

between each type of FIs and geodynamic processes (rifting and subduction).

In Chapter 3, well-preserved transitional characteristics of olivine microstructures and lattice preferred orientations (LPOs) found in the mantle shear zone of the Yugu peridotite body in the Gyeonggi Massif, Korea were reported. Based on their microstructural characteristics (especially olivine grain size), four textural types were classified such as proto-mylonite, proto-mylonite to mylonite transition, mylonite, and ultra-mylonite. Olivine LPO varied with textural type of peridotites, from A-type (proto-mylonites) via D-type (mylonites) to E-type (ultra-mylonites). The olivine fabric transition from A-type to E-type is interpreted to have occurred under hydrous conditions at low temperature (700−760 °C) and high strain, based on characteristics such as Ti-clinohumite defects (and serpentine) and fluid inclusion trails in olivine, and a hydrous mineral (pargasite) in the matrix, especially from the ultra-mylonitic peridotites. However, further geochronological and structural studies are needed to understand the relationship between the ultramafic body and basement rock.

REFERENCES

Andersen, T., Burke, E. A. J. & Neumann, E. R. (1995). Nitrogen-rich fluid in the upper mantle: fluid inclusions in spinel dunite from Lanzarote, Canary Islands. *Contributions to Mineralogy and Petrology* **120**, 20-28.

Andersen, T. & Neumann, E. R. (2001). Fluid inclusions in mantle xenoliths. *Lithos* **55**, 301-320.

Andersen, T., O'Reilly, S. Y. & Griffin, W. L. (1984). The trapped fluid phase in upper mantle xenoliths from Victoria, Australia: implications for mantle metasomatism. *Contributions to Mineralogy and Petrology* **88**, 72-85.

Arai, S., Tamura, A., Ishimaru, S., Kadoshima, K., Lee, Y. I. & Hisada, K. (2008). Petrology of the Yugu peridotites in the Gyeonggi Massif, South Korea: Implications for its origin and hydration process. *Island Arc* **17**, 485-501.

Bachmann, F., Hielscher, R. & Schaeben, H. (2010). Texture analysis with MTEX–free and open source software toolbox. *Solid State Phenomena* **160**, 63-68.

Bakker, R. J. (2003). Package FLUIDS 1. Computer programs for analysis of fluid inclusion data and for modelling bulk fluid properties. *Chemical Geology* **194**, 3-23.

Baldridge, W. S., Damon, P. E., Shafiqullah, M. & Bridwell, R. J. (1980). Evolution of the central Rio Grande rift, New Mexico: New potassium-argon ages. *Earth and Planetary Science Letters* **51**, 309-321.

Ballhaus, C., Berry, R. F. & Green, D. H. (1991). High pressure experimental calibration of the olivine-orthopyroxene-spinel oxygen geobarometer: implications for the oxidation state of the upper mantle. *Contributions to*

Mineralogy and Petrology **107**, 27-40.

Bebout, G. E. (2007). Metamorphic chemical geodynamics of subduction zones. *Earth and Planetary Science Letters* **260**, 373-393.

Bedini, R. M., Bodinier, J. L., Dautria, J. M. & Morten, L. (1997). Evolution of LILE-enriched small melt fractions in the lithospheric mantle: a case study from the East African Rift. *Earth and Planetary Science Letters* **153**, 67-83.

Belkin, H. E. & De Vivo, B. (1989). Glass, phlogopite, and apatite in spinel peridotite xenoliths from Sardinia (Italy): Evidence for mantle metasomatism. *New Mexico Bureau Mines and Mineralogy Research Bulletin* **131**, 20.

Berger, A., Herwegh, M., Schwarz, J.-O. & Putlitz, B. (2011). Quantitative analysis of crystal/grain sizes and their distributions in 2D and 3D. *Journal of Structural Geology* **33**, 1751-1763.

Bergman, S. C. & Dubessy, J. (1984). CO2-CO fluid inclusions in a composite peridotite xenolith: implications for upper mantle oxygen fugacity. *Contributions to Mineralogy and Petrology* **85**, 1-13.

Berkesi, M., Guzmics, T., Szabó, C., Dubessy, J., Bodnar, R. J., Hidas, K. & Ratter, K. (2012). The role of CO2-rich fluids in trace element transport and metasomatism in the lithospheric mantle beneath the Central Pannonian Basin, Hungary, based on fluid inclusions in mantle xenoliths. *Earth and Planetary Science Letters* **331–332**, 8-20.

Berkesi, M., Hidas, K., Guzmics, T., Dubessy, J., Bodnar, R. J., Szabó, C., Vajna, B. & Tsunogae, T. (2009). Detection of small amounts of H2O in CO2-rich fluid inclusions using Raman spectroscopy. *Journal of Raman Spectroscopy* **40**, 1461-1463.

Berkesi, M., Káldos, R., Park, M., Szabó, C., Váczi, T., Török, K., Németh, B. &

Czuppon, G. (2016). Detection of small amounts of N2 in CO2-rich high-density fluid inclusions in mantle xenoliths. *European Journal of Mineralogy*.

Berry, A. J., Hermann, J., O'Neill, H. S. C. & Foran, G. J. (2005). Fingerprinting the water site in mantle olivine. *Geology* **33**, 869-872.

Bodinier, J. L. & Godard, M. (2003). 2.04 - Orogenic, Ophiolitic, and Abyssal Peridotites. In: Holland, H. D. & Turekian, K. K. (eds.) *Treatise on Geochemistry*. Oxford: Pergamon, 1-73.

Bodnar, R. J., Binns, P. R. & Hall, D. L. (1989). Synthetic fluid inclusions - VI. Quantitative evaluation of the decrepitation behaviour of fluid inclusions in quartz at one atmosphere confining pressure. *Journal of Metamorphic Geology* **7**, 229-242.

Brey, G. P. & Köhler, T. (1990). Geothermobarometry in four-phase lherzolites II. New thermobarometers, and practical assessment of existing thermobarometers. *Journal of Petrology* **31**, 1353-1378.

Bunge, H. (1982). Texture Analysis in Materials Science: Mathematical Models. Butteworths, London, 593 pp.

Bürgmann, R. & Dresen, G. (2008). Rheology of the Lower Crust and Upper Mantle: Evidence from Rock Mechanics, Geodesy, and Field Observations. *Annual Review of Earth and Planetary Sciences* **36**, 531-567.

Byerly, B. L. & Lassiter, J. C. (2012). Evidence from mantle xenoliths for lithosphere removal beneath the central Rio Grande Rift. *Earth and Planetary Science Letters* **355–356**, 82-93.

Byerly, B. L. & Lassiter, J. C. (2015). Trace element partitioning and Lu–Hf isotope systematics in spinel peridotites from the Rio Grande Rift and Colorado

Plateau: Towards improved age assessment of clinopyroxene Lu/Hf–176Hf/177Hf in SCLM peridotite. *Chemical Geology* **413**, 146-158.

Bystricky, M., Kunze, K., Burlini, L. & Burg, J.-P. (2000). High Shear Strain of Olivine Aggregates: Rheological and Seismic Consequences. *Science* **290**, 1564-1567.

Cao, Y., Jung, H., Song, S., Park, M., Jung, S. & Lee, J. (2015). Plastic Deformation and Seismic Properties in Fore-arc Mantles: A Petrofabric Analysis of the Yushigou Harzburgites, North Qilian Suture Zone, NW China. *Journal of Petrology* **56**, 1897-1944.

Carter, N. L. & Ave'Lallement, H. G. (1970). High Temperature Flow of Dunite and Peridotite. *Geological Society of America Bulletin* **81**, 2181-2202.

Cho, M., Cheong, W., Ernst, W. G., Yi, K. & Kim, J. (2013). SHRIMP U-Pb ages of detrital zircons in metasedimentary rocks of the central Ogcheon fold-thrust belt, Korea: Evidence for tectonic assembly of Paleozoic sedimentary protoliths. *Journal of Asian Earth Sciences* **63**, 234-249.

Cho, M. & Kim, H. (2005). Petrogenesis of the Yugu spinel harzburgite in western Gyeonggi massif, South Korea. *International Eclogite Conference*. Seggau, Austria, 26.

Cho, M., Kim, Y. & Ahn, J. (2007). Metamorphic Evolution of the Imjingang Belt, Korea: Implications for Permo-Triassic Collisional Orogeny. *International Geology Review* **49**, 30-51.

Choi, D. K. (2014). Geology and Tectonic Evolution of the Korean Peninsula. Seoul National University Press (Korean with English summary), pp.277.

Chough, S. K., Kwon, S. T., Ree, J. H. & Choi, D. K. (2000). Tectonic and sedimentary evolution of the Korean peninsula: a review and new view.

Earth-Science Reviews **52**, 175-235.

Connolly, J. A. D. (2009). The geodynamic equation of state: What and how. *Geochemistry, Geophysics, Geosystems* **10**, Q10014.

Copeland, P., Murphy, M. A., Dupré, W. R. & Lapen, T. J. (2011). Oligocene Laramide deformation in southern New Mexico and its implications for Farallon plate geodynamics. *Geosphere* **7**, 1209-1219.

Dawson, J. B. & Powell, D. G. (1969). Mica in the upper mantle. *Contributions to Mineralogy and Petrology* **22**, 233-237.

Dawson, J. B. & Smith, J. V. (1982). Upper-mantle amphiboles: a review. *Mineralogical Magazine* **45**, 35-46.

De Hoog, J. M., Hattori, K. & Jung, H. (2014). Titanium- and water-rich metamorphic olivine in high-pressure serpentinites from the Voltri Massif (Ligurian Alps, Italy): evidence for deep subduction of high-field strength and fluid-mobile elements. *Contributions to Mineralogy and Petrology* **167**, 1-15.

Dégi, J., Abart, R., Török, K., Rhede, D. & Petrishcheva, E. (2009). Evidence for xenolith–host basalt interaction from chemical patterns in Fe–Ti-oxides from mafic granulite xenoliths of the Bakony–Balaton Volcanic field (W-Hungary). *Mineralogy and Petrology* **95**, 219-234.

Demouchy, S., Tommasi, A., Barou, F., Mainprice, D. & Cordier, P. (2012). Deformation of olivine in torsion under hydrous conditions. *Physics of the Earth and Planetary Interiors* **202**, 56-70.

Dickinson, W. R. & Snyder, W. S. (1978). Plate tectonics of the Laramide orogeny. *Geological Society of America Memoirs* **151**, 355-366.

Dijkstra, A. H., Drury, M. R., Vissers, R. L. M. & Newman, J. (2002). On the role of

melt-rock reaction in mantle shear zone formation in the Othris Peridotite Massif (Greece). *Journal of Structural Geology* **24**, 1431-1450.

Dijkstra, A. H., Drury, M. R., Vissers, R. L. M., Newman, J. & Van Roermund, H. L. M. (2004). Shear zones in the upper mantle: evidence from alpine- and ophiolite-type peridotite massifs. *Geological Society, London, Special Publications* **224**, 11-24.

Drury, M., Vissers, R. M., Van der Wal, D. & Hoogerduijn Strating, E. (1991). Shear localisation in upper mantle peridotites. *Pure and Applied Geophysics* **137**, 439-460.

Falus, G., Tommasi, A. & Soustelle, V. (2011). The effect of dynamic recrystallization on olivine crystal preferred orientations in mantle xenoliths deformed under varied stress conditions. *Journal of Structural Geology* **33**, 1528-1540.

Frey, F. A. & Prinz, M. (1978). Ultramafic inclusions from San Carlos, Arizona: Petrologic and geochemical data bearing on their petrogenesis. *Earth and Planetary Science Letters* **38**, 129-176.

Frezzotti, M.-L. & Touret, J. L. R. (2014). CO2, carbonate-rich melts, and brines in the mantle. *Geoscience Frontiers* **5**, 697-710.

Frezzotti, M. L. (2001). Silicate-melt inclusions in magmatic rocks: applications to petrology. *Lithos* **55**, 273-299.

Frezzotti, M. L., Andersen, T., Neumann, E. R. & Simonsen, S. L. (2002). Carbonatite melt-CO_2 fluid inclusions in mantle xenoliths from Tenerife, Canary Islands: a story of trapping, immiscibility and fluid-rock interaction in the upper mantle. *Lithos* **64**, 77-96.

Frezzotti, M. L., Ferrando, S., Peccerillo, A., Petrelli, M., Tecce, F. & Perucchi, A.

(2010). Chlorine-rich metasomatic H_2O-CO_2 fluids in amphibole-bearing peridotites from Injibara (Lake Tana region, Ethiopian plateau): Nature and evolution of volatiles in the mantle of a region of continental flood basalts. *Geochimica et Cosmochimica Acta* **74**, 3023-3039.

Frezzotti, M. L., Ferrando, S., Tecce, F. & Castelli, D. (2012a). Water content and nature of solutes in shallow-mantle fluids from fluid inclusions. *Earth and Planetary Science Letters* **351–352**, 70-83.

Frezzotti, M. L., Tecce, F. & Casagli, A. (2012b). Raman spectroscopy for fluid inclusion analysis. *Journal of Geochemical Exploration* **112**, 1-20.

Furusho, M. & Kanagawa, K. (1999). Transformation-induced strain localization in a lherzolite mylonite from the Hidaka metamorphic belt of central Hokkaido, Japan. *Tectonophysics* **313**, 411-432.

Gasparik, T. (2000). An Internally Consistent Thermodynamic Model for the System CaO-MgO-Al2O3-SiO2 Derived Primarily from Phase Equilibrium Data. *The Journal of Geology* **108**, 103-119.

Hall, D. L. & Bodnar, R. J. (1989). Comparison of fluid inclusion decrepitation and acoustic emission profiles of Westerly granite and Sioux quartzite. *Tectonophysics* **168**, 283-296.

Handy, M. R. (1989). Deformation regimes and the rheological evolution of fault zones in the lithosphere: the effects of pressure, temperature, grainsize and time. *Tectonophysics* **163**, 119-152.

Hansen, L. N., Zhao, Y.-H., Zimmerman, M. E. & Kohlstedt, D. L. (2014). Protracted fabric evolution in olivine: Implications for the relationship among strain, crystallographic fabric, and seismic anisotropy. *Earth and Planetary Science Letters* **387**, 157-168.

Hansen, L. N., Zimmerman, M. E. & Kohlstedt, D. L. (2011). Grain boundary sliding in San Carlos olivine: Flow law parameters and crystallographic-preferred orientation. *Journal of Geophysical Research: Solid Earth* **116**, B08201.

Hansen, L. N., Zimmerman, M. E. & Kohlstedt, D. L. (2012). The influence of microstructure on deformation of olivine in the grain-boundary sliding regime. *Journal of Geophysical Research: Solid Earth* **117**, B09201.

Hermann, J., Fitz Gerald, J. D., Malaspina, N., Berry, A. J. & Scambelluri, M. (2007). OH-bearing planar defects in olivine produced by the breakdown of Ti-rich humite minerals from Dabie Shan (China). *Contributions to Mineralogy and Petrology* **153**, 417-428.

Herwegh, M., Mercolli, I., Linckens, J. & Müntener, O. (2016). Mechanical anisotropy control on strain localization in upper mantle shear zones. *Tectonics* **35**, 1177-1204.

Hidas, K., Garrido, C. J., Tommasi, A., Padrón-Navarta, J. A., Thielmann, M., Konc, Z., Frets, E. & Marchesi, C. (2013). Strain Localization in Pyroxenite by Reaction-Enhanced Softening in the Shallow Subcontinental Lithospheric Mantle. *Journal of Petrology*.

Hidas, K., Guzmics, T., Szabó, C., Kovács, I., Bodnar, R. J., Zajacz, Z., Nédli, Z., Vaccari, L. & Perucchi, A. (2010). Coexisting silicate melt inclusions and H2O-bearing, CO2-rich fluid inclusions in mantle peridotite xenoliths from the Carpathian–Pannonian region (central Hungary). *Chemical Geology* **274**, 1-18.

Hirth, G. & Kohlstedt, D. L. (1995). Experimental constraints on the dynamics of the partially molten upper mantle: 2. Deformation in the dislocation creep regime. *Journal of Geophysical Research: Solid Earth* **100**, 15441-15449.

Holloway, J. R. & Blank, J. G. (1994). Application of experimental results to COH species in natural melts. *Reviews in Mineralogy and Geochemistry* **30**, 187-230.

Hudson, M. R. & Grauch, V. J. S. (2013). New Perspectives on Rio Grande Rift Basins: From Tectonics to Groundwater (Introduction). *Geological Society of America Special Papers* **494**, v-xii.

Humphreys, E. (2009). Relation of flat subduction to magmatism and deformation in the western United States. *Geological Society of America Memoirs* **204**, 85-98.

Humphreys, E., Hessler, E., Dueker, K., Farmer, G. L., Erslev, E. & Atwater, T. (2003). How Laramide-Age Hydration of North American Lithosphere by the Farallon Slab Controlled Subsequent Activity in the Western United States. *International Geology Review* **45**, 575-595.

Huraiova, M., Dubessy, J. & Konecny, P. (1991). Composition and oxidation state of upper mantle fluids from southern Slovakia. *Plinius* **5**, 110-111.

Izraeli, E. S., Harris, J. W. & Navon, O. (2001). Brine inclusions in diamonds: a new upper mantle fluid. *Earth and Planetary Science Letters* **187**, 323-332.

Jung, H. (2009). Deformation fabrics of olivine in Val Malenco peridotite found in Italy and implications for the seismic anisotropy in the upper mantle. *Lithos* **109**, 341-349.

Jung, H. & Karato, S. (2001a). Water-induced fabric transitions in olivine. *Science* **293**, 1460-1463.

Jung, H. & Karato, S. I. (2001b). Effects of water on dynamically recrystallized grain-size of olivine. *Journal of Structural Geology* **23**, 1337-1344.

Jung, H., Katayama, I., Jiang, Z., Hiraga, I. & Karato, S. (2006). Effect of water and

stress on the lattice-preferred orientation of olivine. *Tectonophysics* **421**, 1-22.

Jung, H., Mo, W. & Choi, S. H. (2009). Deformation microstructures of olivine in peridotite from Spitsbergen, Svalbard and implications for seismic anisotropy. *Journal of Metamorphic Geology* **27**, 707-720.

Jung, S., Jung, H. & Austrheim, H. (2014). Characterization of olivine fabrics and mylonite in the presence of fluid and implications for seismic anisotropy and shear localization. *Earth, Planets and Space* **66**, 1-21.

Kaczmarek, M.-A., Jonda, L. & Davies, H. L. (2015). Evidence of melting, melt percolation and deformation in a supra-subduction zone (Marum ophiolite complex, Papua New Guinea). *Contributions to Mineralogy and Petrology* **170**, 1-23.

Kaczmarek, M.-A. & Reddy, S. M. (2013). Mantle deformation during rifting: Constraints from quantitative microstructural analysis of olivine from the East African Rift (Marsabit, Kenya). *Tectonophysics* **608**, 1122-1137.

Kaczmarek, M. A. & Tommasi, A. (2011). Anatomy of an extensional shear zone in the mantle, Lanzo massif, Italy. *Geochemistry Geophysics Geosystems* **12**.

Kamei, A., Obata, M., Michibayashi, K., Hirajima, T. & Svojtka, M. (2010). Two Contrasting Fabric Patterns of Olivine Observed in Garnet and Spinel Peridotite from a Mantle-derived Ultramafic Mass Enclosed in Felsic Granulite, the Moldanubian Zone, Czech Republic. *Journal of Petrology* **51**, 101-123.

Karato, S. (1987). Scanning electron microscope observation of dislocations in olivine. *Physics and Chemistry of Minerals* **14**, 245-248.

Karato, S., Jung, H., Katayama, I. & Skemer, P. (2008). Geodynamic significance of

seismic anisotropy of the upper mantle: New insights from laboratory studies. *Annual Review of Earth and Planetary Sciences* **36**, 59-95.

Karato, S.-I. & Jung, H. (2003). Effects of pressure on high-temperature dislocation creep in olivine. *Philosophical Magazine* **83**, 401-414.

Karato, S.-I., Paterson, M. S. & FitzGerald, J. D. (1986). Rheology of synthetic olivine aggregates: Influence of grain size and water. *Journal of Geophysical Research: Solid Earth* **91**, 8151-8176.

Karato, S.-i., Toriumi, M. & Fujii, T. (1980). Dynamic recrystallization of olivine single crystals during high-temperature creep. *Geophysical Research Letters* **7**, 649-652.

Katayama, I., Jung, H. & Karato, S. I. (2004). New type of olivine fabric from deformation experiments at modest water content and low stress. *Geology* **32**, 1045-1048.

Katayama, I. & Karato, S. (2006). Effect of temperature on the B- to C-type olivine fabric transition and implication for flow pattern in subduction zones. *Physics of the Earth and Planetary Interiors* **157**, 33-45.

Katayama, I., Kurosaki, I. & Hirauchi, K. (2010). Low silica activity for hydrogen generation during serpentinization: An example of natural serpentinites in the Mineoka ophiolite complex, central Japan. *Earth and Planetary Science Letters* **298**, 199-204.

Kawamoto, T., Kanzaki, M., Mibe, K., Matsukage, K. N. & Ono, S. (2012). Separation of supercritical slab-fluids to form aqueous fluid and melt components in subduction zone magmatism. *Proceedings of the National Academy of Sciences of the United States of America* **109**, 18695-18700.

Kawamoto, T., Yoshikawa, M., Kumagai, Y., Mirabueno, M. H. T., Okuno, M. &

Kobayashi, T. (2013). Mantle wedge infiltrated with saline fluids from dehydration and decarbonation of subducting slab. *Proceedings of the National Academy of Sciences* **110**, 9663-9668.

Keppler, H. (2013). Volatiles under High Pressure. *Physics and Chemistry of the Deep Earth*: John Wiley & Sons, Ltd, 1-37.

Khisina, N. R., Wirth, R., Andrut, M. & Ukhanov, A. V. (2001). Extrinsic and intrinsic mode of hydrogen occurrence in natural olivines: FTIR and TEM investigation. *Physics and Chemistry of Minerals* **28**, 291-301.

Kil, Y. & Wendlandt, R. F. (2004). Pressure and temperature evolution of upper mantle under the Rio Grande rift. *Contributions to Mineralogy and Petrology* **148**, 265-280.

Kil, Y. & Wendlandt, R. F. (2007). Depleted and enriched mantle processes under the Rio Grande rift: spinel peridotite xenoliths. *Contributions to Mineralogy and Petrology* **154**, 135-151.

Kim, H., Cho, M. & Kim, J. (2003). Evidence for mantle deformation from the Yugu Peridotite: A Preliminary Study. *The Geological Society of Korea*, 23-23.

Kim, S. W., Oh, C. W., Williams, I. S., Rubatto, D., Ryu, I. C., Rajesh, V. J., Kim, C. B., Guo, J. H. & Zhai, M. G. (2006). Phanerozoic high-pressure eclogite and intermediate-pressure granulite facies metamorphism in the Gyeonggi Massif, South Korea: Implications for the eastward extension of the Dabie-Sulu continental collision zone. *Lithos* **92**, 357-377.

Kitamura, M., Kondoh, S., Morimoto, N., Miller, G. H., Rossman, G. R. & Putnis, A. (1987). Planar OH-bearing defects in mantle olivine. *Nature* **328**, 143-145.

Konzett, J., Krenn, K., Rubatto, D., Hauzenberger, C. & Stalder, R. (2014). The

formation of saline mantle fluids by open-system crystallization of hydrous silicate-rich vein assemblages – Evidence from fluid inclusions and their host phases in MARID xenoliths from the central Kaapvaal Craton, South Africa. *Geochimica et Cosmochimica Acta* **147**, 1-25.

Kwon, S., Sajeev, K., Mitra, G., Park, Y., Kim, S. W. & Ryu, I. C. (2009). Evidence for Permo-Triassic collision in Far East Asia: The Korean collisional orogen. *Earth and Planetary Science Letters* **279**, 340-349.

Kyser, T. K. & Rison, W. (1982). Systematics of rare gas isotopes in basic lavas and ultramafic xenoliths. *Journal of Geophysical Research: Solid Earth* **87**, 5611-5630.

Lee, C. T. A. (2005). Trace element evidence for hydrous metasomatism at the base of the North American lithosphere and possible association with Laramide low-angle subduction. *Journal of Geology* **113**, 673-685.

Lee, S. R., Cho, M., Hwang, J. H., Lee, B.-J., Kim, Y.-B. & Kim, J. C. (2003). Crustal evolution of the Gyeonggi massif, South Korea: Nd isotopic evidence and implications for continental growths of East Asia. *Precambrian Research* **121**, 25-34.

Leeman, W. P. (1982). Tectonic and magmatic significance of strontium isotopic variations in Cenozoic volcanic rocks from the western United States. *Geological Society of America Bulletin* **93**, 487-503.

Linckens, J., Herwegh, M. & Müntener, O. (2015). Small quantity but large effect — How minor phases control strain localization in upper mantle shear zones. *Tectonophysics* **643**, 26-43.

Linckens, J., Herwegh, M., Muntener, O. & Mercolli, I. (2011). Evolution of a polymineralic mantle shear zone and the role of second phases in the

localization of deformation. *Journal of Geophysical Research-Solid Earth* **116**.

Litasov, K. D., Shatskiy, A. & Ohtani, E. (2013). Earth's Mantle Melting in the Presence of C–O–H–Bearing Fluid. *Physics and Chemistry of the Deep Earth*: John Wiley & Sons, Ltd, 38-65.

Mackwell, S. J., Kohlstedt, D. L. & Paterson, M. S. (1985). The role of water in the deformation of olivine single crystals. *Journal of Geophysical Research: Solid Earth* **90**, 11319-11333.

Matsyuk, S. S. & Langer, K. (2004). Hydroxyl in olivines from mantle xenoliths in kimberlites of the Siberian platform. *Contributions to Mineralogy and Petrology* **147**, 413-437.

McCallister, R. H. & Yund, R. A. (1977). Coherent exsolution in Fe-free pyroxenes. *American Mineralogist* **62**, 721-726.

Mehl, L., Hacker, B. R., Hirth, G. & Kelemen, P. B. (2003). Arc-parallel flow within the mantle wedge: Evidence from the accreted Talkeetna arc, south central Alaska. *Journal of Geophysical Research: Solid Earth* **108**, 2375.

Mei, S., Bai, W., Hiraga, T. & Kohlstedt, D. L. (2002). Influence of melt on the creep behavior of olivine–basalt aggregates under hydrous conditions. *Earth and Planetary Science Letters* **201**, 491-507.

Menzies, M., Rogers, N., Tindell, A. & Hawkesworth, C. (1987). METASOMATIC AND ENRICHMENT PROCESSES IN LITHOSPHERIC PERIDOTITES, AN EFFECT OF ASTHENOSPHERE-LITHOSPHERE. *Mantle Metasomatism: Academic Press Monograph Series*. UK, 312-364.

Michibayashi, K. & Mainprice, D. (2004). The Role of Pre-existing Mechanical Anisotropy on Shear Zone Development within Oceanic Mantle Lithosphere:

an Example from the Oman Ophiolite. *Journal of Petrology* **45**, 405-414.

Michibayashi, K. & Oohara, T. (2013). Olivine fabric evolution in a hydrated ductile shear zone at the Moho Transition Zone, Oman Ophiolite. *Earth and Planetary Science Letters* **377–378**, 299-310.

Murck, B., Burruss, R. & Hollister, L. (1978). Phase equilibria in fluid inclusions in ultramafic xenoliths. *American Mineralogist* **63**, 40-46.

Newman, J., Lamb, W. M., Drury, M. R. & Vissers, R. L. M. (1999). Deformation processes in a peridotite shear zone: reaction-softening by an H_2O-deficient, continuous net transfer reaction. *Tectonophysics* **303**, 193-222.

Nimis, P. & Grütter, H. (2010). Internally consistent geothermometers for garnet peridotites and pyroxenites. *Contributions to Mineralogy and Petrology* **159**, 411-427.

O'Reilly, S. Y. & Griffin, W. L. (2000). Apatite in the mantle: implications for metasomatic processes and high heat production in Phanerozoic mantle. *Lithos* **53**, 217-232.

Oh, C. W., Kim, S. W., Choi, S. G., Zhai, M. G., Guo, J. H. & Krishnan, S. (2005). First finding of eclogite facies metamorphic event in South Korea and its correlation with the Dabie-Sulu collision belt in China. *Journal of Geology* **113**, 226-232.

Oh, C. W. & Kusky, T. (2007). The late permian to triassic hongseong-odesan collision belt in south Korea, and its tectonic correlation with China and Japan. *International Geology Review* **49**, 636-657.

Oh, C. W., Seo, J., Choi, S. G., Rajesh, V. J. & Lee, J. H. (2012). U-Pb SHRIMP zircon geochronology, petrogenesis, and tectonic setting of the Neoproterozoic Baekdong ultramafic rocks in the Hongseong Collision Belt,

South Korea. *Lithos* **128**, 100-112.

Palasse, L. N., Vissers, R. L. M., Paulssen, H., Basu, A. R. & Drury, M. R. (2012). Microstructural and seismic properties of the upper mantle underneath a rifted continental terrane (Baja California): An example of sub-crustal mechanical asthenosphere? *Earth and Planetary Science Letters* **345**, 60-71.

Park, M., Jung, H. & Kil, Y. (2014). Petrofabrics of olivine in a rift axis and rift shoulder and their implications for seismic anisotropy beneath the Rio Grande rift. *Island Arc* **23**, 299-311.

Pasteris, J. D. (1987). Fluid inclusions in mantle xenoliths. *Mantle xenoliths*, 691-707.

Peacock, S. A. (1990). Fluid processes in subduction zones. *Science* **248**, 329-337.

Pintér, Z., Patkó, L., Tene Djoukam, J. F., Kovács, I., Tchouankoue, J. P., Falus, G., Konc, Z., Tommasi, A., Barou, F., Mihály, J., Németh, C. & Jeffries, T. (2015). Characterization of the sub-continental lithospheric mantle beneath the Cameroon volcanic line inferred from alkaline basalt hosted peridotite xenoliths from Barombi Mbo and Nyos Lakes. *Journal of African Earth Sciences* **111**, 170-193.

Porreca, C., Selverstone, J. & Samuels, K. (2006). Pyroxenite xenoliths from the Rio Puerco volcanic field, New Mexico: Melt metasomatism at the margin of the Rio Grande rift. *Geosphere* **2**, 333-351.

Precigout, J., Gueydan, F., Gapais, D., Garrido, C. J. & Essaifi, A. (2007). Strain localisation in the subcontinental mantle — a ductile alternative to the brittle mantle. *Tectonophysics* **445**, 318-336.

Putnis, A. (1992). *An introduction to mineral sciences*: Cambridge University Press.

Ree, J.-H., Cho, M., Kwon, S.-T. & Nakamura, E. (1996). Possible eastward

extension of Chinese collision belt in South Korea: The Imjingang belt. *Geology* **24**, 1071-1074.

Ricketts, J. W., Kelley, S. A., Karlstrom, K. E., Schmandt, B., Donahue, M. S. & van Wijk, J. (2016). Synchronous opening of the Rio Grande rift along its entire length at 25–10 Ma supported by apatite (U-Th)/He and fission-track thermochronology, and evaluation of possible driving mechanisms. *Geological Society of America Bulletin* **128**, 397-424.

Ringwood, A. E. (1979). Origin of the Earth and Moon. *New York, Springer-Verlag New York, Inc., 1979. 307 p.* **1**.

Roden, M. F., Irving, A. J. & Murthy, V. R. (1988). Isotopic and trace element composition of the upper mantle beneath a young continental rift: Results from Kilbourne Hole, New Mexico. *Geochimica et Cosmochimica Acta* **52**, 461-473.

Roedder, E. (1965). Liquid CO2 inclusions in olivine-bearing nodules and phenocrysts from basalts. *American Mineralogist* **50**, 1746-1782.

Roedder, E. (1984). Fluid inclusions. *Reviews in Mineralogy* **12**, 1-646.

Rowe, M. C. & Lassiter, J. C. (2009). Chlorine enrichment in central Rio Grande Rift basaltic melt inclusions: Evidence for subduction modification of the lithospheric mantle. *Geology* **37**, 439-442.

Rowe, M. C., Lassiter, J. C. & Goff, K. (2015). Basalt volatile fluctuations during continental rifting: An example from the Rio Grande Rift, USA. *Geochemistry, Geophysics, Geosystems* **16**, 1254-1273.

Sachan, H. K., Mukherjee, B. K. & Bodnar, R. J. (2007). Preservation of methane generated during serpentinization of upper mantle rocks: Evidence from fluid inclusions in the Nidar ophiolite, Indus Suture Zone, Ladakh (India).

Earth and Planetary Science Letters **257**, 47-59.

Sánchez-Muñoz, L., del Campo, A. & Fernández, J. F. (2016). Symmetry constraints during the development of anisotropic spinodal patterns. *Scientific Reports* **6**, 20806.

Sawaguchi, T. (2004). Deformation history and exhumation process of the Horoman Peridotite Complex, Hokkaido, Japan. *Tectonophysics* **379**, 109-126.

Scambelluri, M. & Philippot, P. (2001). Deep fluids in subduction zones. *Lithos* **55**, 213-227.

Schiano, P. & Clocchiatti, R. (1994). Worldwide occurrence of silica-rich melts in sub-continental and sub-oceanic mantle minerals. *Nature* **368**, 621-624.

Schiano, P., Clocchiatti, R. & Joron, J. L. (1992). Melt and fluid inclusions in basalts and xenoliths from Tahaa Island, Society archipelago: evidence for a metasomatized upper mantle. *Earth and Planetary Science Letters* **111**, 69-82.

Seo, J., Oh, C. W., Choi, S. G. & Rajesh, V. J. (2013). Two ultramafic rock types in the Hongseong area, South Korea: Tectonic significance for northeast Asia. *Lithos* **175–176**, 30-39.

Severinghaus, J. & Atwater, T. (1990). Cenozoic geometry and thermal state of the subducting slabs beneath western North America. *Geological Society of America Memoirs* **176**, 1-22.

Skemer, P., Katayama, I., Jiang, Z. & Karato, S. (2005). The misorientation index: Development of a new method for calculating the strength of lattice-preferred orientation. *Tectonophysics* **411**, 157-167.

Skemer, P., Warren, J. M., Hansen, L. N., Hirth, G. & Kelemen, P. B. (2013). The influence of water and LPO on the initiation and evolution of mantle shear

zones. *Earth and Planetary Science Letters* **375**, 222-233.

Skemer, P., Warren, J. M., Kelemen, P. B. & hirth, G. (2010). Microstructural and Rheological Evolution of a Mantle Shear Zone. *Journal of Petrology* **51**, 43-53.

Smith, D. (2000). Insights into the evolution of the uppermost continental mantle from xenolith localities on and near the Colorado Plateau and regional comparisons. *Journal of Geophysical Research-Solid Earth* **105**, 16769-16781.

Smith, D., Riter, J. C. A. & Mertzman, S. A. (1999). Water-rock interactions, orthopyroxene growth, and Si-enrichment in the mantle: evidence in xenoliths from the Colorado Plateau, southwestern United States. *Earth and Planetary Science Letters* **165**, 45-54.

Soustelle, V., Tommasi, A., Demouchy, S. & Ionov, D. A. (2010). Deformation and Fluid–Rock Interaction in the Supra-subduction Mantle: Microstructures and Water Contents in Peridotite Xenoliths from the Avacha Volcano, Kamchatka. *Journal of Petrology* **51**, 363-394.

Spengler, D., Obata, M., Hirajima, T., Ottolini, L., Ohfuji, H., Tamura, A. & Arai, S. (2012). Exsolution of Garnet and Clinopyroxene from High-Al Pyroxenes in Xugou Peridotite, Eastern China. *Journal of Petrology* **53**, 1477-1504.

Szabó, C. & Bodnar, R. J. (1996). Changing Magma Ascent Rates in the Nógrád-Gömör Volcanic Field Northern Hungary/Southern Slovakia: Evidence from CO_2-Rich Fluid Inclusions in Metasomatized Upper Mantle Xenoliths. *Petrology* **4**, 221-230.

Szabó, C., Hidas, K., Bali, E., Zajacz, Z., Kovács, I., Yang, K., Guzmics, T. & Török, K. (2009). Melt–wall rock interaction in the mantle shown by silicate melt

inclusions in peridotite xenoliths from the central Pannonian Basin (western Hungary). *Island Arc* **18**, 375-400.

Tasaka, M., Zimmerman, M. E. & Kohlstedt, D. L. (2016). Evolution of the rheological and microstructural properties of olivine aggregates during dislocation creep under hydrous conditions. *Journal of Geophysical Research: Solid Earth* **121**, 92-113.

Taylor, W. R. & Green, D. H. (1988). Measurement of reduced peridotite-COH solidus and implications for redox melting of the mantle. *Nature* **332**, 349-352.

Tommasi, A., Mainprice, D., Canova, G. & Chastel, Y. (2000). Viscoplastic self-consistent and equilibrium-based modeling of olivine lattice preferred orientations: implications for the upper mantle seismic anisotropy. *Journal of Geophysical Research* **105**, 7893-7908.

Tommasi, A., Tikoff, B. & Vauchez, A. (1999). Upper mantle tectonics: three-dimensional deformation, olivine crystallographic fabrics and seismic properties. *Earth and Planetary Science Letters* **168**, 173-186.

Tommasi, A., Vauchez, A., Godard, M. & Belley, F. (2006). Deformation and melt transport in a highly depleted peridotite massif from the Canadian Cordillera: Implications to seismic anisotropy above subduction zones. *Earth and Planetary Science Letters* **252**, 245-259.

Török, K. & De Vivo, B. (1995). Fluid inclusions in upper mantle xenoliths from the Balaton Highland, Western Hungary. *Acta Vulcanologica* **7**, 277-284.

van den Kerkhof, A. M. (1988). The system CO2-CH4-N2 in fluid inclusions: theoretical modelling and geological applications. Ph.D. Dissertation Free University Amsterdam, 209 pp. .

Van den Kerkhof, A. M. & Hein, U. F. (2001). Fluid inclusion petrography. *Lithos* **55**, 27-47.

Van der Wal, D., Chopra, P., Drury, M. & Gerald, J. F. (1993). Relationships between dynamically recrystallized grain size and deformation conditions in experimentally deformed olivine rocks. *Geophysical Research Letters* **20**, 1479-1482.

Vissers, R. L. M., Drury, M. R., Newman, J. & Fliervoet, T. F. (1997). Mylonitic deformation in upper mantle peridotites of the North Pyrenean Zone (France): implications for strength and strain localization in the lithosphere. *Tectonophysics* **279**, 303-325.

Viti, C. & Frezzotti, M. L. (2000). Re-equilibration of glass and CO2 inclusions in xenolith olivine: A TEM study. *American Mineralogist* **85**, 1390-1396.

Wanamaker, B. J. & Evans, B. (1989). Mechanical re-equilibration of fluid inclusions in San Carlos olivine by power-law creep. *Contributions to Mineralogy and Petrology* **102**, 102-111.

Warren, J. M. & Hirth, G. (2006). Grain size sensitive deformation mechanisms in naturally deformed peridotites. *Earth and Planetary Science Letters* **248**, 438-450.

Warren, J. M., Hirth, G. & Kelemen, P. B. (2008). Evolution of olivine lattice preferred orientation during simple shear in the mantle. *Earth and Planetary Science Letters* **272**, 501-512.

Wells, P. R. A. (1977). Pyroxene thermometry in simple and complex systems. *Contributions to Mineralogy and Petrology* **62**, 129-139.

Witt-Eickschen, G. & Seck, H. A. (1991). Solubility of Ca and Al in orthopyroxene from spinel peridotite: an improved version of an empirical geothermometer.

Contributions to Mineralogy and Petrology **106**, 431-439.

Woo, Y. K. & Cho, Y. H. (2002). Ultramafic Rocks of Yoogoo Talc Ore Deposits Area, Choongnam, Korea. *Report of Science Education* **33**, 29-42.

Wyllie, P. J. & Ryabchikov, I. D. (2000). Volatile components, magmas, and critical fluids in upwelling mantle. *Journal of Petrology* **41**, 1195-1206.

Yamamoto, J., Kagi, H., Kaneoka, I., Lai, Y., Prikhod'ko, V. S. & Arai, S. (2002). Fossil pressures of fluid inclusions in mantle xenoliths exhibiting rheology of mantle minerals: implications for the geobarometry of mantle minerals using micro-Raman spectroscopy. *Earth and Planetary Science Letters* **198**, 511-519.

Yamamoto, J., Otsuka, K., Ohfuji, H., Ishibashi, H., Hirano, N. & Kagi, H. (2011). Retentivity of CO2 in fluid inclusions in mantle minerals. *European Journal of Mineralogy* **23**, 805-815.

Zhang, S. & Karato, S. (1995). Lattice preferred orientation of olivine aggregates deformed in simple shear. *Nature* **375**, 774-777.

Zhang, S., Karato, S.-i., Fitz Gerald, J., Faul, U. H. & Zhou, Y. (2000). Simple shear deformation of olivine aggregates. *Tectonophysics* **316**, 133-152.

Zimmerman, M. E. & Kohlstedt, D. L. (2004). Rheological Properties of Partially Molten Lherzolite. *Journal of Petrology* **45**, 275-298.

ABSTRACT IN KOREAN (국문초록)

지구의 최상부 층에 해당하는 암석권은 지각과 상부 맨틀로 구성되어 있으며, 특히 암석권 맨틀은 물리-화학적으로 지각의 뿌리를 이루는 공간이다. 맨틀 기원의 감람암은 상부 맨틀의 물리-화학적 성질(맨틀 교대작용 및 변형작용)에 대한 중요한 정보를 제공해 줄 수 있으므로, 이러한 연구는 지구의 지화학적 및 유동학적 진화 과정을 이해하는데 중요한 역학을 한다.

본 박사학위 논문에서는 미국 뉴 멕시코 주 리오 그란드 리프트(Rio Grande Rift) 및 우리나라 경기육괴 유구 지역의 자연 상에서 변형된 감람암에서 나타나는 변형 미세구조와 유체포유물의 진화사를 이해하기 위해 다양한 분석기기들(주사전자현미경, 후방산란전자회절, 전자현미분석기, 적외선-라만 분광기, 집속이온빔장비, 히팅-쿨링 스테이지 등)을 사용하였다.

미국 뉴 멕시코 주 리오 그란트 리프트 서쪽 가장자리에 있는 Adam’s Diggings지역에 분포하는 알칼리 현무암에 포획된 다섯 개의 첨정석 감람암을 채취하였다. 유체포유물의 암석기재학적 특징에 따라 두 가

지 다른 유형의 집합체인 Type-1 및 Type-2 유체포유물들이 사방휘석에 분포하는 것을 확인하였다. 암석기재학적 특징과 다양한 분석결과들에 따르면 이러한 두 가지 유체포유물들의 형성 시기와 조성이 확연히 다르다는 것을 발견하였다. 이와 같은 결과들은 리오 그란드 리프트 맨틀 내에서 서로 다른 압력(깊이)과 유체 조성(CO_2-N_2 vs CO_2-H_2O)을 가진 유체 침입이 적어도 두 번 있었다는 것을 나타내며, 이들의 유체 특징을 종합적으로 고려하였을 때 각각 서로 다른 "환원 및 산화 환경"을 지시하는 것으로 여겨진다. 따라서, 초기의 유체 침범(Type-1)은 사방휘석의 용리 박막층(exsolution lamellae)이 형성되기 직전 혹은 형성되는 과정 동안에 "C-O-N-S"의 유체 조성이 침투되었으며, 이와 같은 용리 박막층과 초기의 "Type-1 유체포유물"이 형성된 이후에 "C-O-H-S"의 유체 조성이 침투되어 "Type-2 유체포유물"이 형성되었을 것으로 생각된다. 이러한 두 가지의 서로 다른 유체 성분 특성(환원 및 산화 환경)과 이들의 진화사에 관한 연구결과는 이 지역의 맨틀교대작용과 맨틀 유체의 복잡성(맨틀의 지화학적 불균질성)에 관한 중요한 시사점을 제시하였다.

우리나라 경기육괴에 속한 유구 감람암체의 맨틀 전단대 지역에서 나

타나는 다양한 미세구조와 감람석의 격자선호방향(LPO), 그리고 변형 당시 물의 존재 유무에 관심을 가지고 본 연구를 수행하였다. 유구 감람암체는 대부분 첨정석 하즈버자이트로 이루어져 있으며, 러졸라이트 두나이트, 휘석암 등도 함께 나타난다. 감람암의 변형된 미세구조를 바탕으로 이들을 원압쇄암, 원압쇄암-압쇄암의 전이단계, 압쇄암, 초압쇄암의 네 가지 유형으로 분류하였다. 흥미롭게도 감람석의 격자선호방향이 이러한 미세구조의 형태에 따라 원압쇄암(A-type), 압쇄암(D-type), 초압쇄암(E-type)으로 점진적으로 변화하는 사실을 발견하였다. 특히, 초압쇄암에서 특징적으로 나타나는 함수광물 및 유체포유물 등의 증거를 바탕으로 볼 때, 유구 감람암이 초압쇄암화 작용을 받는 과정에서 물과 함께 상대적으로 저온 및 고변형 작용 하에서 형성되었을 것으로 해석된다. 이와 같은 학위논문의 결과들을 통해 상부 맨틀에서 나타나는 지화학적-유동학적 불균질성에 대한 체계적인 이해가 증진될 것으로 기대한다.

주요어: 감람암, 유체포유물, 미세구조, 맨틀교대작용, 맨틀진화, 맨틀의 불균질성

학 번: 2011-30116